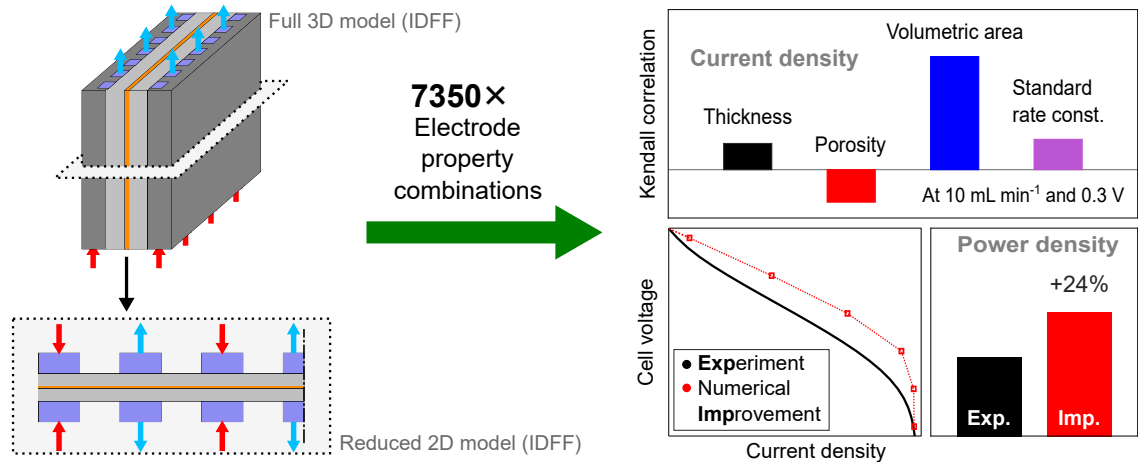


Graphical Abstract

Data-Driven Electrode Parameter Identification for Vanadium Redox Flow Batteries Through Experimental and Numerical Methods

Ziqiang Cheng, Kevin M. Tenny, Alberto Pizzolato, Antoni Forner-Cuenca, Vittorio Verda, Yet-Ming Chiang, Fikile R. Brushett, Reza Behrou



Highlights

Data-Driven Electrode Parameter Identification for Vanadium Redox Flow Batteries Through Experimental and Numerical Methods

Ziqiang Cheng, Kevin M. Tenny, Alberto Pizzolato, Antoni Forner-Cuenca, Vittorio Verda, Yet-Ming Chiang, Fikile R. Brushett, Reza Behrou

- A computationally expensive 3D VRFB model is reduced to a 2D model
- The 2D model is experimentally and numerically validated
- A full parametric sweep is performed based on 2D simulation results
- Quantitative correlations are established from system non-linearities
- Correlations provide the basis for electrode design improvements

Data-Driven Electrode Parameter Identification for Vanadium Redox Flow Batteries Through Experimental and Numerical Methods

Ziqiang Cheng^{a,1}, Kevin M. Tenny^{b,1}, Alberto Pizzolato^a, Antoni Forner-Cuenca^c, Vittorio Verda^a, Yet-Ming Chiang^d, Fikile R. Brushett^{b,*}, Reza Behrou^{e,*}

^a*Department of Energy, Politecnico di Torino, Turin, Italy*

^b*Department of Chemical Engineering, Massachusetts Institute of Technology, Cambridge, MA, USA*

^c*Department of Chemical Engineering and Chemistry, Eindhoven University of Technology, Eindhoven, The Netherlands*

^d*Department of Materials Science and Engineering, Massachusetts Institute of Technology, Cambridge, MA, USA*

^e*Department of Mechanical and Aerospace Engineering, University of California San Diego, La Jolla, CA, USA*

Abstract

The vanadium redox flow battery (VRFB) is a promising energy storage technology for stationary applications (e.g., renewables integration) that offers a pathway to cost-effectiveness through independent scaling of power and energy as well as longevity. Many current research efforts are focused on improving battery performance through electrode modifications, but high-throughput, laboratory-scale testing can be time- and material-intensive. Advances in multiphysics-based numerical modeling and data-driven parameter identification afford a computational platform to expand the design space by rapidly screening a diverse array of electrode configurations. Herein, a 3D VRFB model is first developed and validated against experimental results. Subsequently, a new 2D model is composed, yielding a computationally-light simulation framework, which is used to span bounded values of the electrode thickness, porosity, volumetric area, fiber diameter, and kinetic rate constant across six cell polarization voltages. This generates a dataset of 7350 electrode property combinations for each cell voltage, which is used to evaluate the effect of these structural properties on the pressure drop and current density. These structure-performance relationships are further quantified using Kendall τ rank correlation coefficients to highlight the dependence of cell performance on bulk electrode morphology and to identify improved property sets. This statistical framework may serve as a general guideline for parameter identification for more advanced electrode designs and redox flow battery (RFB) stacks.

*Corresponding authors:

Email addresses: brushett@mit.edu (Fikile R. Brushett), rbehrou@eng.ucsd.edu (Reza Behrou)

¹Equal contribution.

Keywords: Vanadium redox flow batteries (VRFBs), Interdigitated flow field (IDFF), Electrode parametric study, Data-driven modeling, Numerical modeling, Experimental validation

Nomenclature

List of symbols

\dot{v}	scan rate [V s^{-1}]
\mathcal{F}	Faraday constant [A s mol^{-1}]
\mathcal{R}	universal gas constant [$\text{J mol}^{-1} \text{K}^{-1}$]
\tilde{C}_{ref}	model surface capacitance (geometric area) [F m^{-2}]
C_e	electrode capacitance [F]
D	diffusivity [$\text{m}^2 \text{s}^{-1}$]
d_f	mean fiber diameter [m]
D_h	hydraulic diameter [m]
E_{eq}	equilibrium potential [V]
E_{oc}	open-circuit potential [V]
H	thickness [m]
I_{EDLC}	EDLC-measured current [A]
I_{ox}	oxidative current [A]
I_{red}	reductive current [A]
k	standard rate constant [m s^{-1}]
k_{CK}	Carman-Kozeny constant [-]
L	electrode or channel length [m]
p^*	pressure at the entrance of an outlet channel [Pa]
Q	volumetric flow rate [$\text{m}^3 \text{s}^{-1}$]

R	reaction rate [$\text{mol m}^{-3} \text{s}^{-1}$] or fluid flow resistance [$\text{kg m}^{-4} \text{s}^{-1}$]
S	source term [$\text{mol m}^{-3} \text{s}^{-1}$]
S_d	dissociation rate [$\text{mol m}^{-3} \text{s}^{-1}$]
W	electrode width [m]
w	width [m]
\bar{c}	x -averaged concentration [mol m^{-3}]
\bar{p}	x -averaged pressure [Pa]
Δp	pressure drop [Pa]
i_l	ionic current density entering the liquid phase (local area) [A m^{-2}]
i_s	electronic current density leaving the solid phase (local area) [A m^{-2}]
\mathbf{N}	molar flux [$\text{mol m}^{-2} \text{s}^{-1}$]
\mathbf{n}	outward unit normal vector [-]
\mathbf{u}	velocity vector [m s^{-1}]
\bar{M}	intermediate quantities used to estimate the surface concentrations [-]
\bar{P}	intermediate quantities used to estimate the surface concentrations [-]
a	exponent parameter for mass transfer coefficient [-]
A_M	surface area per mass [$\text{m}^2 \text{kg}^{-1}$]
A_V	volumetric area [$\text{m}^2 \text{m}^{-3}$]
b	pre-factor parameter for mass transfer coefficient [-]
c	molar concentration [mol m^{-3}]
I	current [A]
i	current density (geometric area) [A m^{-2}]
i_0	exchange current density (local area) [A m^{-2}]
i_{loc}	local current density (local area) [A m^{-2}]
k_m	mass transfer coefficient [m s^{-1}]

m_e	electrode mass [kg]
N	number of channels for each half-cell [-]
n	number of electrons transferred [-]
P	discharge power [W m^{-2}]
p	pressure [Pa]
T	temperature [K]
U_{cell}	cell voltage [V]
x	coordinate in channel length direction [m]
y	coordinate in channel width direction [m]
z	coordinate in cell thickness direction [m], or charge number [-]
Be	Bejan number [-]
Re	Reynolds number [-]

Greek symbols

α	charge transfer coefficient [-]
η	overpotential [V]
Γ	boundaries [-]
κ	permeability [m^2]
λ	stoichiometric coefficient [-]
ν	kinematic viscosity [$\text{m}^2 \text{s}^{-1}$]
Ω	computational domains [-]
σ_l	ionic conductivity [S m^{-1}]
σ_s	electronic conductivity [S m^{-1}]
θ	number of electrode segments [-]
μ	viscosity [Pa.s]
ϕ_l	electric potential in the liquid phase [V]

ϕ_s	electric potential in the solid phase [V]
ψ_{pump}	pump energy conversion factor [-]
ρ	density [kg m^{-3}]
τ	Kendall correlation coefficient [-]
ε	porosity [-]
Ξ	cell pumping power [W]
ξ	intermediate quantity used to estimate pressure drop [-]
ζ	cell power efficiency [-]

Superscripts

0	initial condition
eff	effective quantity
s	liquid-solid interface
l	uncompressed

Subscripts

+	positive
-	negative
0	standard quantity
a	anodic
c	cathodic
i	species, excluding SO_4^{2-}
j	species, including SO_4^{2-}
l	liquid phase
s	solid phase
t	positive or negative, $t \in \{+, -\}$
ch	channels

<i>ele</i>	electrode
<i>e</i>	electrode
<i>in</i>	inlet
<i>mem</i>	membrane
<i>out</i>	outlet
ref	reference quantity

Abbreviations

CV	Cyclic voltammogram
EDLC	Electrochemical double-layer capacitance
IDFF	Interdigitated flow field
MRE	Mean relative error
OCV	Open circuit voltage
PFF	Parallel flow field
RFB	Redox flow battery
RMSE	Root-mean-square error
SFF	Serpentine flow field
SOC	State-of-charge
VRFB	Vanadium redox flow battery

1. Introduction

Reliable integration of variable renewable energy sources into current electric power infrastructure continues to be a challenge for cost-effective grid decarbonization [1]. In particular, the intermittency of solar and wind generation spans timescales incongruent with daily power demands and thus requires complementary energy storage systems for uninterrupted operation [2, 3]. Redox flow batteries (RFBs) are a nascent electrochemical technology anticipated to enable more effective

use of renewable energy sources [4]. This technology offers independent scaling of stored energy through active species concentration and tank size as well as the discharge power through the reactor area [5]. Vanadium redox flow batteries (VRFBs), the current state-of-the-art embodiment, possess excellent operational flexibility [6] and design modularity [7], chemical reversibility [8], and long life cycle [8] making them suitable for grid-scale energy storage applications [6]. However, their high capital costs and limited power and energy density still prevent widespread market penetration [8-10] motivating further research into component optimization.

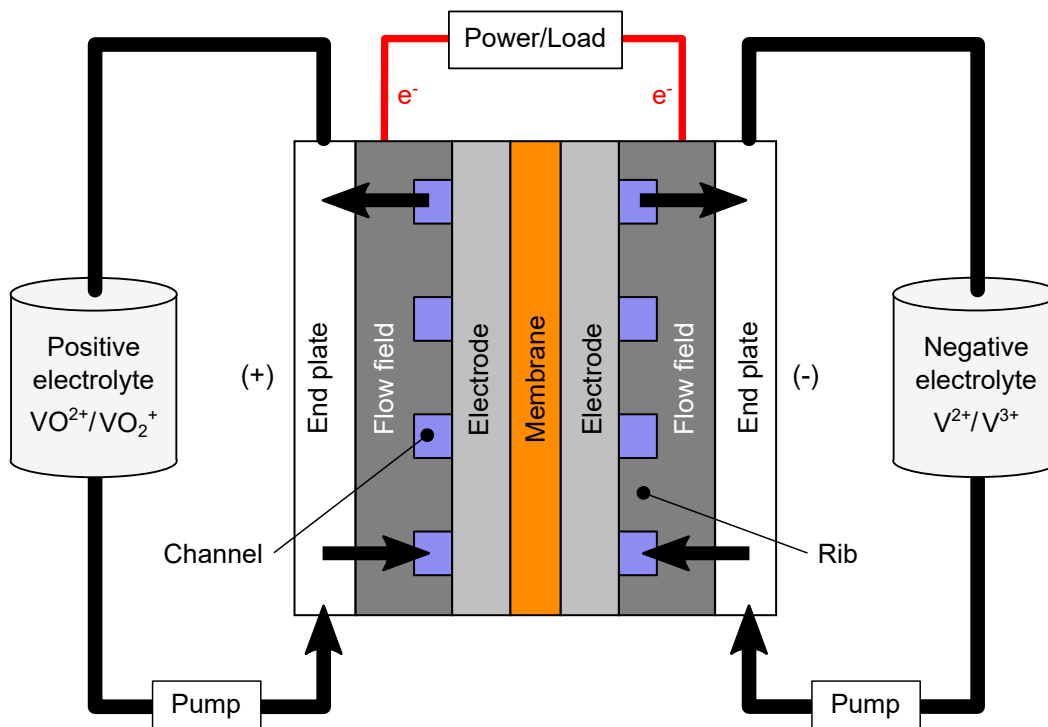
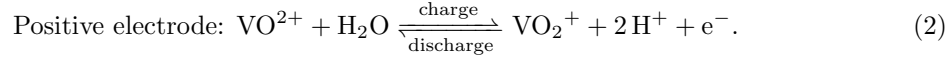
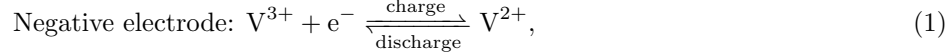


Figure 1: Schematic representation of a typical single-cell VRFB.

The VRFB interconverts electrical energy and chemical energy by oxidizing and reducing soluble vanadium cations [11, 12]. A schematic representation of a typical single-cell VRFB is shown in Fig. 1. The positive and negative electrolyte reservoirs are external of the electrochemical flow cell and the electrolytes are pumped through the reactor. Within the cell, an ion exchange membrane serves as a selective barrier preventing electrolyte cross-over, while permitting proton transport [13]. A range of flow fields (e.g., serpentine flow field (SFF), parallel flow field (PFF), and interdigitated

flow field (IDFF)) are used to distribute electrolytes across the surface of the porous electrodes [14]. The electrodes provide electrochemically active surfaces for the following redox reactions [15]:



Electrodes play several important roles in the VRFB [16-20] including: i) facilitating the electrochemical reaction kinetics during charge/discharge through surface reactions; ii) impacting cell resistance through material conductivity; iii) enabling the battery lifetime through the chemical stability in highly oxidizing positive electrolytes; and iv) influencing the pumping loss through their permeability and porosity [17]. In general, pristine electrode surfaces have sluggish kinetics prompting various pretreatment strategies to improve the reaction rate [20, 21], such as thermal and chemical oxidations and nitrogenizations [8, 15-17]. In addition to augmenting kinetics, these strategies can also enhance electrode surface area further improving performance [22]. Both the reaction rate and the surface area are intuitive properties to modify as they impact the electron flux from the redox reactions at the electrode surface. The electrode thickness also plays a significant role in the electrochemical performance [23] and the pressure drop in the cell [24], which can be modulated by abutting multiple single electrode layers. Finally, studies in the electrode porosity and permeability reveal connections to the peak power [25], accessible energy density [26], energy efficiency [26-29], and fluid dynamics [30]. In whole, electrode modifications continue to be a targeted research area to improve the overall VRFB electrochemical performance [22, 27, 31-39]. However, while the electrode structure-performance relationship can be elucidated with systematic experimental analyses, these campaigns can be time-, labor-, and resource-intensive. Furthermore, diverse electrode screening is restricted by commercially available materials or access to in-house fabrication tools, which limits the breadth and depth of possible electrode morphologies.

Numerical modeling offers an alternative platform to study the impact of component property profiles, engendered by flow field configurations and electrode materials, on the electrochemical and the fluid dynamic responses of the RFB cells. These simulations typically require measured, fitted, or referenced chemical property data in addition to specified governing equations and geometric dimensions for establishing the computational domain. Three-dimensional (3D) RFB models have been developed and compared to experimental results [14, 40-47]. However, given the various feature lengths in a RFB, 3D model are computationally expensive, which has, in turn, motivated

the development of two-dimensional (2D) RFB models to more quickly compare simulation results with lab-scale cells [48-57]. These 2D models are generally created by omitting the influence of one spatial dimension in the RFB, which can result in inaccurate cell-level fluid dynamic values [58]. Indeed, when compared to the 3D models, 2D simulations sacrifice accuracy for computational lightness in order to perform myriad calculations in a short amount of time. Nevertheless, some 2D RFB models have been leveraged for parametric analysis of various cell properties [59, 60], which are unaffected by inaccuracies in fluid dynamics. Consequently, the parametric sweeps in these studies yielded large data sets from which additional quantitative relationships could have also been drawn. To the best of our knowledge, the electrode properties in previous studies have not considered a quantitative correlative impact on RFB electrochemical and fluid dynamic performance.

Herein, this paper presents a comprehensive integrated experimental and numerical approach to study the impact of different electrode properties—thickness, porosity, fiber diameter, volumetric area, and standard rate constant—on cell performance in a systematic fashion at different cell voltages. A lab-scale VRFB cell is constructed to measure electrochemical properties; subsequently, a full 3D single-cell model and a new reduced 2D model based on the experimental configuration are developed and validated against the experimental results. Our 2D model offers a computationally inexpensive approach and a robust approximation of the overall cell performance as evinced by the similarities between the simulated and experimental polarization curves. We further calibrated the performance of the 2D model through an in-depth comparison of the 2D and 3D characteristic responses in velocity, pressure, concentration, solid- and liquid-phase electric potential, and overpotential. A bounded parametric sweep considering all electrode property combinations is performed using the 2D model resulting in a simulation dataset of 7350 electrode configurations at six different cell voltages. Statistical correlations between these parameters and the electrochemical and hydrodynamic outputs are computed to quantify the relative influence of each parameter on the cell performance. Finally, we conclude by simulating an improved theoretical electrode, based on the parametric sweep and statistical assessment, using cell electrochemical and pumping power values to motivate continued work in electrode development.

2. Physical models

The physical models presented in this paper describe the governing physical phenomena and reaction kinetics in the electrodes, electrolytes, and membrane for both 3D and 2D configurations.

The physical phenomena include conservation of mass, species, momentum, and charge as well as reaction kinetics that describes the fluid dynamic and electrochemical responses in a single-cell VRFB. To simplify the computational complexity, the following assumptions are made:

- (1) Steady-state iso-thermal conditions are assumed for all physical processes;
- (2) The electrolytes are assumed to be incompressible;
- (3) Hydrogen and oxygen evolution are neglected in both electrodes;
- (4) Only protons are assumed to pass through the membrane;
- (5) Dilute solution approximation is used [61];
- (6) All material properties are assumed to be isotropic and homogeneous;
- (7) All contact resistances between the electrodes and the flow fields are neglected;
- (8) Potential losses in the flow fields and end plates are neglected due to their high electronic conductivity.

The computational domain for the 3D full-cell model is illustrated in Fig. 2a. The domain includes the channels (Ω_{ch}), electrodes (Ω_e), and membrane (Ω_{mem}). The inlets (Γ_{in}) and outlets (Γ_{out}) are illustrated as arrows and dotted lines in Fig. 2a and Fig. 2b, respectively. In Fig. 2a, $z_1 - z_6$ are referred to the z -coordinates for different interfaces.

2.1. 3D model

2.1.1. Conservation of mass

The conservation of mass in both free flow channels, Ω_{ch} , and porous electrodes, Ω_e , is described by the continuity equation:

$$\nabla \cdot \mathbf{u} = 0, \quad (3)$$

where \mathbf{u} is the electrolyte velocity field and $\nabla \cdot (\cdot) = \partial(\cdot)_i / \partial x_i$ is the divergence of a field.

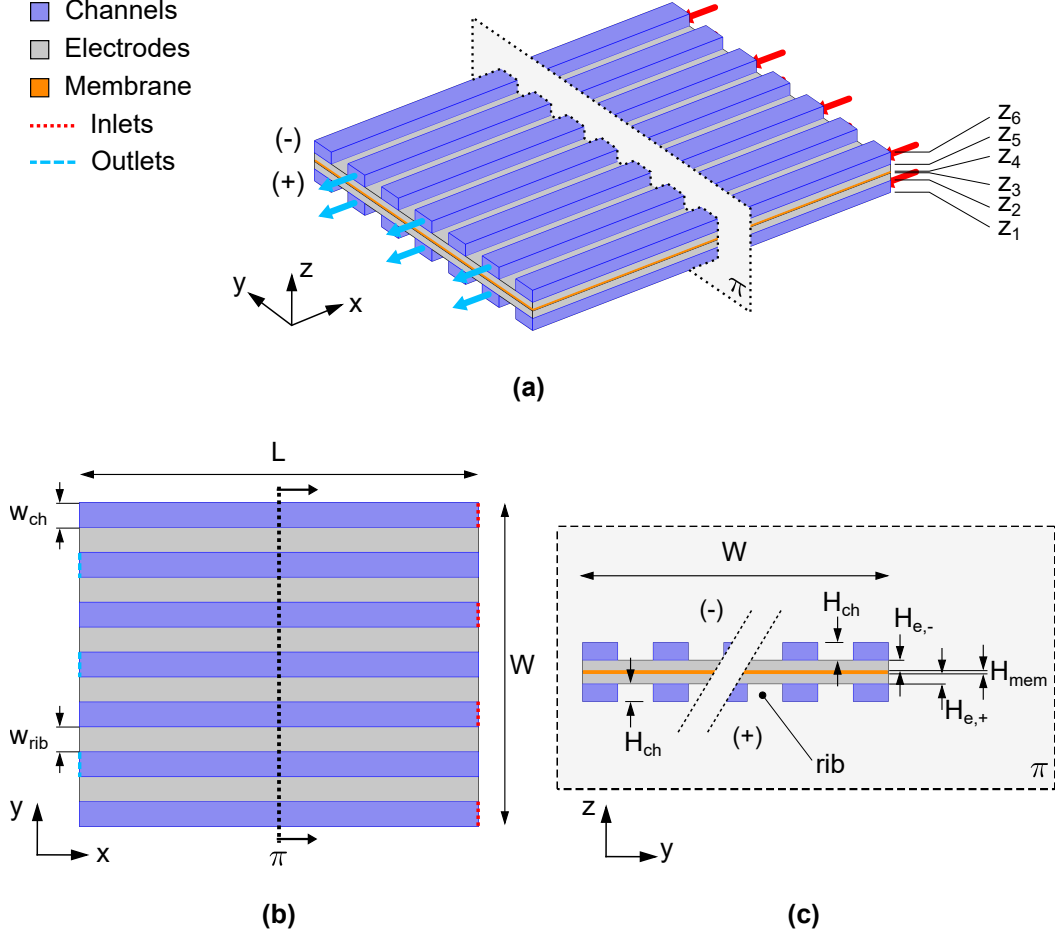


Figure 2: Schematic representations of: (a) the computational domain for the 3D model, (b) the top view of the domain, and (c) an arbitrary cross section of the domain on the yz plane.

2.1.2. Conservation of momentum

The conservation of momentum in the free flow channels, Ω_{ch} , is described by the incompressible Navier-Stokes equation [62]:

$$\rho(\mathbf{u} \cdot \nabla) \mathbf{u} = -\nabla p + \mu \nabla^2 \mathbf{u}, \quad (4)$$

where ρ is the electrolyte density, p is the pressure field, μ is the electrolyte viscosity, and $\nabla(\cdot) = \partial(\cdot)_i / \partial x_j$ is the gradient of a field. In the porous electrodes, Ω_e , the Brinkman equation is adopted

to describe the conservation of momentum as follows [63]:

$$\frac{\rho}{\varepsilon} \left((\mathbf{u} \cdot \nabla) \frac{\mathbf{u}}{\varepsilon} \right) = -\nabla p + \frac{\mu}{\varepsilon} \nabla^2 \mathbf{u} - \frac{\mu}{\kappa} \mathbf{u}, \quad (5)$$

where ε and κ are the electrode porosity and the permeability, respectively. Compared to the most commonly-used Darcy's law, the Brinkman equation considers the kinetic energy loss due to the viscous shear forces and allows the no-slip condition at the walls [63, 64]. Furthermore, it is simpler to solve the partial differential equations as the equation has similar form as the Navier-Stokes equation in the free-flow channels [64].

The permeability is estimated by Carman-Kozeny equation [65]:

$$\kappa = \frac{d_f^2 \varepsilon^3}{16k_{CK} (1 - \varepsilon)^2}, \quad (6)$$

where d_f is the mean fiber diameter in the electrode and k_{CK} is the Carman-Kozeny constant [65].

2.1.3. Species transport

In our model, the contribution of V^{2+} , V^{3+} , VO^{2+} , VO_2^+ , H^+ , HSO_4^- , and SO_4^{2-} , are considered in the solution. The electrochemical transport of species in the electrolytes is governed by the conservation of mass [61]:

$$\nabla \cdot \mathbf{N}_i = S_i \quad \text{with} \quad S_i = R_i + S_{d,i}, \quad (7)$$

where $i \in \{V^{2+}, V^{3+}, VO^{2+}, VO_2^+, H^+, HSO_4^-\}$, \mathbf{N}_i is the concentration flux of the i^{th} species, S_i are the source terms that include the reaction rates (R_i) and the dissociation rates ($S_{d,i}$). The concentration flux that describes the transport mechanisms in the electrolytes is defined by the modified Nernst-Planck equation [61]:

$$\mathbf{N}_i = -\frac{z_i c_i D_i^{\text{eff}}}{\mathcal{R}T} \mathcal{F} \nabla \phi_l - D_i^{\text{eff}} \nabla c_i + c_i \mathbf{u} \quad (8)$$

where \mathcal{R} and \mathcal{F} are the respective universal gas and Faraday constants, T is the absolute temperature, ϕ_l is the electric potential in the liquid phase, c_i is the molar concentration, z_i is the charge number, and D_i^{eff} is the effective diffusivity computed as follows:

$$\begin{cases} D_i^{\text{eff}} = D_i & \text{in } \Omega_{ch}, \\ D_i^{\text{eff}} = D_i \varepsilon^{1.5} & \text{in } \Omega_e. \end{cases} \quad (9)$$

For the electrodes (Ω_e), the diffusivity is modified by the electrode porosity through the Bruggeman correction [66], where D_i is the nominal molecular diffusivity. We note that SO_4^{2-} is not included in Eqs. (7) and (8) as the concentration of SO_4^{2-} is determined by solution electroneutrality as follows:

$$\sum_j z_j c_j = 0, \quad (10)$$

where z_j is the charge number and j includes SO_4^{2-} and all species given in Eq. (7).

2.1.4. Reaction kinetics

The reactions occur at the liquid-solid interface of the porous electrodes, where active species—including $\text{V}^{2+}/\text{V}^{3+}$ and $\text{VO}_2^+/\text{VO}^{2+}$ for the respective negative and positive electrodes—are generated or consumed during the interfacial reactions. This leads to mass transport between the bulk electrolyte and the interface; thus, the reaction rate is controlled partially by the charge transfer and partially by the reactant supply [67, 68]. To this end, a modified concentration-dependent Butler-Volmer equation, which considers the interplay between the mass transfer and the charge transfer effects [55], is used as follows [49, 50, 69]:

$$i_{loc,-} = i_{0,-} \left[\frac{c_{V3}^s}{c_{V3}} \exp\left(-\frac{\alpha_{c,-} n \mathcal{F} \eta_-}{\mathcal{R} T}\right) - \frac{c_{V2}^s}{c_{V2}} \exp\left(\frac{\alpha_{a,-} n \mathcal{F} \eta_-}{\mathcal{R} T}\right) \right], \quad (11)$$

$$i_{loc,+} = i_{0,+} \left[\frac{c_{V5}^s}{c_{V5}} \exp\left(-\frac{\alpha_{c,+} n \mathcal{F} \eta_+}{\mathcal{R} T}\right) - \frac{c_{V4}^s}{c_{V4}} \exp\left(\frac{\alpha_{a,+} n \mathcal{F} \eta_+}{\mathcal{R} T}\right) \right], \quad (12)$$

where i_{loc} and i_0 refer to the respective local current density and exchange current density, α_a and α_c are the respective anodic and cathodic charge transfer coefficients, n is the number of electrons transferred when an electrochemical reaction occurs ($n=1$), η is the overpotential, and c_i^s is the surface concentration at the liquid-solid interface with $i \in \{V_2, V_3, V_4, V_5\}$. The subscripts V_2 , V_3 , V_4 , and V_5 refer to V^{2+} , V^{3+} , VO^{2+} , and VO_2^+ , respectively, and the subscripts “−” and “+” correspond to the negative and positive electrodes, respectively. The exchange current densities are given by [49, 66]:

$$i_{0,-} = \mathcal{F} k_- c_{V2}^{\alpha_{c,-}} c_{V3}^{\alpha_{a,-}}, \quad (13)$$

$$i_{0,+} = \mathcal{F} k_+ c_{V4}^{\alpha_{c,+}} c_{V5}^{\alpha_{a,+}}, \quad (14)$$

where k_- and k_+ are the standard rate constants for the negative and positive reactions, respectively. The overpotentials are defined as [61]:

$$\eta_- = \phi_s - \phi_l - E_{oc,-}, \quad (15)$$

$$\eta_+ = \phi_s - \phi_l - E_{oc,+}, \quad (16)$$

where ϕ_s is the electric potential in the solid phase, and $E_{oc,t}$ is the open circuit voltage (OCV) for the t^{th} reaction ($t \in \{-, +\}$). The OCV is estimated by the Nernst equation; however, we note that there are several different forms of this equation that result in different predictions of $E_{oc,t}$. A discrepancy of ca. 131–140 mV can be observed when the simplified Nernst equation typical of fuel cell literature is used [48, 49]. As discussed by Knehr and Kumbur this is due to the exclusion of the Donnan potential at the membrane-electrolyte interfaces and the variation in proton concentration during operation [70]. As such, we adopt a modified Nernst equation given by:

$$E_{oc,-} = E_{0,-} + \frac{\mathcal{R}T}{n\mathcal{F}} \ln \left(\frac{c_{V3}}{c_{V2}} \right), \quad (17)$$

$$E_{oc,+} = E_{0,+} + \frac{\mathcal{R}T}{n\mathcal{F}} \ln \left(\frac{c_{V5} (c_{H,+})^2}{c_{V4}} \right), \quad (18)$$

where $E_{0,-}$ and $E_{0,+}$ are the standard equilibrium potentials for the respective negative and positive reactions, and the second term in the right-hand-side considers the effect of temperature and species concentrations [70, 71]. As suggested in previous work [50, 70], when determining the proton concentration in Eq. (18), the sulfuric acid is assumed to be fully dissociated. Thus, it is given as $c_{H,+} = c_{H,+}^{ini} + c_{V5}$ with $c_{H,+}^{ini}$ being the initial proton concentration of the positive electrolyte at a state-of-charge (SOC) of zero. The SOC is defined as follows:

$$\text{SOC} = \frac{c_{V2}}{c_{V2} + c_{V3}} = \frac{c_{V5}}{c_{V4} + c_{V5}}. \quad (19)$$

Notably, the concentrations given in Eqs. (17) and (18) are in $[\text{mol L}^{-1}]$ instead of $[\text{mol m}^{-3}]$ since the concentrations are derived from chemical activities. Unless otherwise stated, all units are presented in the Nomenclature section.

The reaction rates, R_i , can be computed from the local current density by Faraday's law as follows [61]:

$$R_i = \frac{\lambda_i A_V i_{loc}}{n\mathcal{F}}, \quad (20)$$

where A_V is the volumetric area and λ_i is the dimensionless stoichiometric coefficient in the corresponding half reactions. In this work, we assume the stoichiometric coefficient is positive for reducing species and negative for oxidizing species [61].

2.1.5. Sulfuric acid dissociation

The dissociation of sulfuric acid (H_2SO_4) in the electrolyte, in both Ω_{ch} and Ω_e , includes two steps:



According to Knopf et al. [72], H_2SO_4 is completely dissociated for concentration less than 40 mol kg^{-1} at temperature between 273 and 323 K. This range includes the electrolyte solutions used in this paper. Therefore, the first step (Eq. (21)) is assumed to be complete for all the cases considered in this model. The second step is described by a dissociation source term as reported in [50]:

$$S_d = k_d \left(\frac{c_{\text{H}} - c_{\text{HSO}_4}}{c_{\text{H}} + c_{\text{HSO}_4}} - \beta \right), \quad (23)$$

where β is the degree of dissociation of HSO_4^- and k_d is the dissociation rate constant. The source terms, S_i , are obtained by combining the dissociation rate, S_d , and reaction rates, R_i , as summarized in Table 1.

Table 1: Source terms, S_i , for species transport given in Eq. (7).

Species	Negative	Positive
V^{2+}	$A_V i_{loc}/n\mathcal{F}$	—
V^{3+}	$-A_V i_{loc}/n\mathcal{F}$	—
VO^{2+}	—	$A_V i_{loc}/n\mathcal{F}$
VO_2^+	—	$-A_V i_{loc}/n\mathcal{F}$
H^+	$-S_d$	$-S_d - 2A_V i_{loc}/n\mathcal{F}$
HSO_4^-	S_d	S_d

2.1.6. Local mass transfer

The surface concentration of the i^{th} species, c_i^s , is estimated from the corresponding bulk concentration, c_i , through the local mass transport between the interface and bulk electrolyte as follows [49]:

$$k_m (c_i - c_i^s) = -\frac{\lambda_i i_{loc}}{n\mathcal{F}}, \quad (24)$$

where k_m is the mass transfer coefficient. For a given electrode and electrolyte, the mass transfer coefficient is given by [73]:

$$k_m = b |\mathbf{u}|^a, \quad (25)$$

where a and b are empirical constants as describing in Section 4.2. Combining Eqs. (11), (12) and (24) gives the surface concentrations of the vanadium ions as follows [49]:

$$c_{V2}^s = \frac{\bar{P}_- c_{V3} + (1 + \bar{P}_-) c_{V2}}{1 + \bar{M}_- + \bar{P}_-}, \quad c_{V3}^s = \frac{\bar{M}_- c_{V2} + (1 + \bar{M}_-) c_{V3}}{1 + \bar{M}_- + \bar{P}_-}, \quad (26)$$

$$c_{V4}^s = \frac{\bar{P}_+ c_{V5} + (1 + \bar{P}_+) c_{V4}}{1 + \bar{M}_+ + \bar{P}_+}, \quad c_{V5}^s = \frac{\bar{M}_+ c_{V4} + (1 + \bar{M}_+) c_{V5}}{1 + \bar{M}_+ + \bar{P}_+}, \quad (27)$$

where

$$\bar{M}_- = \frac{k_-}{nk_m} (c_{V2})^{-\alpha_{a,-}} (c_{V3})^{\alpha_{a,-}} \exp\left(\frac{\alpha_{a,-} n\mathcal{F}\eta_-}{\mathcal{R}T}\right), \quad (28)$$

$$\bar{P}_- = \frac{k_-}{nk_m} (c_{V2})^{\alpha_{c,-}} (c_{V3})^{-\alpha_{c,-}} \exp\left(-\frac{\alpha_{c,-} n\mathcal{F}\eta_-}{\mathcal{R}T}\right), \quad (29)$$

$$\bar{M}_+ = \frac{k_+}{nk_m} (c_{V4})^{-\alpha_{a,+}} (c_{V5})^{\alpha_{a,+}} \exp\left(\frac{\alpha_{a,+} n\mathcal{F}\eta_+}{\mathcal{R}T}\right), \quad (30)$$

$$\bar{P}_+ = \frac{k_+}{nk_m} (c_{V4})^{\alpha_{c,+}} (c_{V5})^{-\alpha_{c,+}} \exp\left(-\frac{\alpha_{c,+} n\mathcal{F}\eta_+}{\mathcal{R}T}\right). \quad (31)$$

2.1.7. Conservation of charge

The conservation of charge states that the total current is conserved throughout the electrodes, Ω_e , and channels, Ω_{ch} :

$$\nabla \cdot (\mathbf{i}_s + \mathbf{i}_l) = 0, \quad (32)$$

where \mathbf{i}_s is the electronic current density leaving the solid phase and \mathbf{i}_l is the ionic current density entering the liquid phase. Assuming the reaction occurs at the interface, the balance of charge for each phase gives:

$$\nabla \cdot \mathbf{i}_s = -\nabla \cdot \mathbf{i}_l = A_V i_{loc}. \quad (33)$$

The ionic current density is carried by migration and diffusion of species defined as follows [61]:

$$\mathbf{i}_l = \mathcal{F} \sum_i z_i \left(-\frac{z_i c_i D_i^{\text{eff}} \mathcal{F}}{\mathcal{R}T} \nabla \phi_l - D_i^{\text{eff}} \nabla c_i \right). \quad (34)$$

The electronic current density is described by Ohm's law [61]:

$$\mathbf{i}_s = -\sigma_{s,e}^{\text{eff}} \nabla \phi_s, \quad (35)$$

where the effective electrode electronic conductivity, $\sigma_{s,e}^{\text{eff}}$, is obtained through the Bruggeman correction [48]:

$$\sigma_{s,e}^{\text{eff}} = \sigma_{s,e} (1 - \varepsilon)^{1.5}, \quad (36)$$

where $\sigma_{s,e}$ is the nominal electrode electronic conductivity. In the membrane, Ω_{mem} , the electronic current density becomes zero and the ionic current density is carried by protons as follows:

$$\nabla \cdot \mathbf{i}_{l,mem} = 0, \quad (37)$$

where $\mathbf{i}_{l,mem}$ is the membrane ionic current density given by an equivalent Ohm's law [61]:

$$\mathbf{i}_{l,mem} = -\sigma_{l,mem} \nabla \phi_{l,mem}, \quad (38)$$

with $\sigma_{l,mem}$ that is referred to the ionic conductivity of the membrane and $\phi_{l,mem}$ is the liquid-phase electric potential in the membrane.

2.2. Boundary conditions

In this section, the boundary conditions for a single-cell VRFB, given in Fig. 2 are defined. At the inlets, the flow rate and the molar concentrations are given by:

$$-\int_{\Gamma_{in}} \mathbf{u} \cdot \mathbf{n} dS = Q \quad \text{on } \Gamma_{in}, \quad (39)$$

$$c_i = c_{i,in} \quad \text{on } \Gamma_{in}, \quad (40)$$

where Q is the given volumetric flow rate, dS indicates the surface integral, \mathbf{n} is the outward unit normal vector, and $c_{i,in}$ is the inlet concentration of the i^{th} species. It is assumed that $c_{i,in}$ is equal to the corresponding initial concentration, i.e., c_i^0 , of the electrolytes measured in experiments. At the outlets, the pressure is set to zero and the flow is assumed to be fully developed:

$$p_{out} = 0 \text{ Pa} \quad \text{on } \Gamma_{out}, \quad (41)$$

$$-\mathbf{n} \cdot \nabla c_i = 0 \quad \text{on } \Gamma_{out}. \quad (42)$$

At the exterior walls, no-slip [63] and no-flux conditions are specified:

$$\mathbf{u} = 0 \quad \text{on } \Gamma_{wall}, \quad (43)$$

$$-\mathbf{n} \cdot \mathbf{N}_i = 0 \quad \text{on } \Gamma_{wall}, \quad (44)$$

where the exterior walls boundary, Γ_{wall} , is defined as $\Gamma_{tot}/(\Gamma_{in} \cup \Gamma_{out})$ with Γ_{tot} being all the boundaries for the negative and positive half-cells excluding the membrane.

Additionally, an insulation condition is applied for both ionic and electronic current densities at all boundaries except the rib-electrode and membrane-electrode interfaces:

$$-\mathbf{n} \cdot \mathbf{i}_l = 0, \quad -\mathbf{n} \cdot \mathbf{i}_s = 0 \quad \text{on } \Gamma_{tot}/(\Gamma_{rib|e} \cup \Gamma_{mem|e}), \quad (45)$$

where $\Gamma_{rib|e}$ refers to the rib-electrode interfaces (at z_2 and z_5 for positive and negative half-cells), and $\Gamma_{mem|e}$ refers to the membrane-electrode interfaces (at z_3 and z_4 for positive and negative half-cells) in Fig. 2a.

At the channel-electrode interfaces ($\Gamma_{ch|e}$ with $z = z_2, z_5$), we assume that the electronic current cannot be transferred in the electrolyte. Hence, an insulation condition is applied only for the electronic current density:

$$-\mathbf{n} \cdot \mathbf{i}_s = 0 \quad \text{on } \Gamma_{ch|e}. \quad (46)$$

At the negative, $\Gamma_{rib|e,-}$, and the positive, $\Gamma_{rib|e,+}$, rib-electrode interfaces, as stated in the last assumption listed in Section 2 the electric potentials in the solid phase are assumed to be given [14]:

$$\phi_s = \begin{cases} 0 \text{ V} & \text{on } \Gamma_{rib|e,-}, \\ U_{cell} & \text{on } \Gamma_{rib|e,+}, \end{cases} \quad (47)$$

$$(48)$$

where U_{cell} is the given cell voltage. At the membrane-electrode interfaces, the current density fluxes are continuous; however, we note that no electronic current density can be transferred across the membrane. A continuous boundary condition can be applied to the ionic current densities as follows:

$$\mathbf{n} \cdot \mathbf{i}_l = \mathbf{n} \cdot \mathbf{i}_{l,mem} \quad \text{on } \Gamma_{mem|e}. \quad (49)$$

Since only the protons can pass through the membrane, the current density over the entire membrane-electrode interface is described by proton concentration flux as follows:

$$\mathbf{n} \cdot \mathbf{N}_H = \frac{\mathbf{n} \cdot \mathbf{i}_l}{\mathcal{F}} \quad \text{on } \Gamma_{mem|e}. \quad (50)$$

Furthermore, a liquid-phase potential shift is presented across the membrane-electrode interface due to the proton concentration difference [50, 70]. The potential shift is computed by the Donnan potential [74] as follows:

$$\phi_l - \phi_{l,mem} = -\frac{\mathcal{R}T}{\mathcal{F}} \ln \left(\frac{c_H}{c_{H,mem}} \right) \quad \text{on } \Gamma_{mem|e}, \quad (51)$$

where $c_{H,mem}$ is the proton concentration in the membrane calculated from electroneutrality [75]:

$$c_{H,mem} = -z_f c_f, \quad (52)$$

with z_f and c_f being the charge number and the concentration of the fixed charge sites in the membrane, respectively. As reported in previous studies [48, 76], c_f is set to 1200 mol m^{-3} and assumed to be constant throughout the process.

2.3. 2D model

To alleviate the computational complexity of the full 3D model, a new 2D model is also developed. Our 2D model incorporates the averaging effect of the outlet pressure through a reliable approximation, which will be discussed (*vide infra*). This allows the 2D model to properly capture the polarization curve and fluid dynamic responses of the full 3D model. A schematic representation of the 2D model in an arbitrary cross section in the yz plane of Fig. 2 is shown as Fig. 3, where $\Gamma_{in,2D}$, $\Gamma_{out,2D}$, and $\Gamma_{wall,2D}$ indicate the inlets, outlets, and walls, respectively. The symmetric boundary, Γ_{sym} , is used to simplify the computational domain due to symmetry along the y axis in the cell.

For the 2D model, apart from the assumptions listed in Section 2, variations of the scalar field quantities, i.e., pressure, concentrations, overpotentials, electric potentials, in the direction of the channel length (x direction) are assumed to be negligible; whereas, for the vectorial quantities such as the velocity field, the components in the yz plane are assumed to be constant in the x direction. The directions are defined in Fig. 2. The components in the yz plane for the entities are emphasized since the x direction is neglected in the reduced model. We note that this assumption is based on

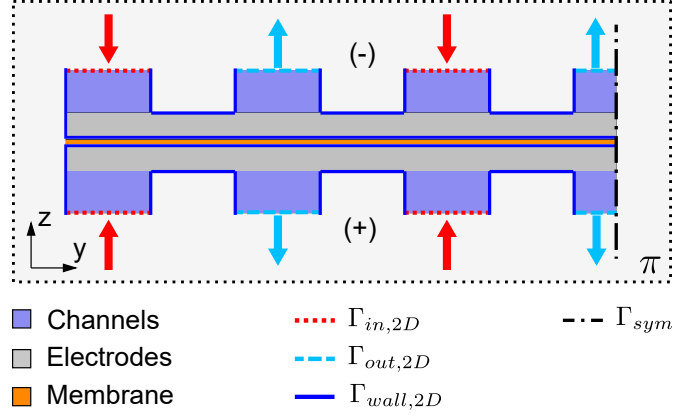


Figure 3: Schematic representation of the computational domain for the 2D model.

the special characteristics of IDFF, and further examinations might be required for alternate flow fields.

For the 2D physical modeling, all 3D governing equations (Eqs. (3)–(38)) remain valid. Whereas for the boundary conditions, only the fully developed flow at the outlets and those related to the exterior walls, current densities, and electric potentials (Eqs. (42)–(51)) still hold. As shown in Fig. 3, the inlets and the outlets are assumed to be the interfaces between the channel and flow field. The geometric characteristics of the IDFF force electrolytes in channels to pass through the porous electrode [59, 77]. Hence, a modified flow rate condition is applied as follows:

$$-\int_{\Gamma_{in,2D}} (\mathbf{u} \cdot \mathbf{n}) L ds = \frac{Q}{2} \quad \text{on } \Gamma_{in,2D}, \quad (53)$$

where ds refers to the line integral over the inlet boundary. The flow rate, Q , is halved since only one half of the model is studied due to the symmetry boundary condition. $\int_{\Gamma_{in,2D}} L ds$ is referred to the corresponding channel area in the xy direction.

At Γ_{sym} , the symmetric boundary conditions are applied [62]:

$$\mathbf{u} \cdot \mathbf{n} = 0 \quad \text{on } \Gamma_{sym}, \quad (54)$$

$$-\mathbf{n} \cdot \mathbf{N}_i = 0 \quad \text{on } \Gamma_{sym}. \quad (55)$$

Theoretically, the 3D inlet concentration condition, Eq. (40), should be modified as:

$$c_i = \bar{c}_{i,in} \quad \text{on } \Gamma_{in,2D}, \quad (56)$$

where $\bar{c}_{i,in}$ refers to the x -averaged 3D concentration at the corresponding channel-flow field interfaces, at z_1 and z_6 for positive and negative half-cells, respectively (Fig. 2a). It can be shown from the 3D simulations that $\bar{c}_{i,in}$ is close to $c_{i,in}$ with relative discrepancies smaller than 0.1% for cell voltage from 0.1 V to the model OCV (1.35 V). Therefore, the 3D inlet concentration condition (Eq. 40) still holds for the 2D model.

Similarly, an x -averaged 3D outlet pressure condition is applied:

$$p_{out,2D} = \bar{p}_{out} \quad \text{on} \quad \Gamma_{out,2D}, \quad (57)$$

where \bar{p}_{out} refers to the corresponding x -averaged 3D pressure. Unless otherwise stated, $p_{(\cdot)}$ stands for 3D pressure.

To estimate the value of \bar{p}_{out} , we performed a full 3D simulation and extracted the streamlines to study how the electrolyte flows from inlets to outlets, as shown in Fig. 4a. Thereafter, we put emphasis on an arbitrary unit-channel pair composed of an inlet channel, an outlet channel, and a porous electrode between the two channels, as depicted in Fig. 4b. It can be seen that the fluid predominately flows in x direction in channels and y direction in the under-rib electrode, which is in agreement with the assumption given in Ref. 78.

To this end, we estimate the pressure distribution along the channels assuming the unit inlet-outlet channel pair consists of several identical segments in x direction (i.e., θ segments for the electrode portion, and $(\theta - 1)$ for each channel). We further developed an analogous equivalent circuit model as shown in Fig. 4c, where the volumetric flow rate, pressure, and fluid flow resistance are equivalent to electric current, potential, and resistance, respectively 79. Compared to the computational fluid dynamics simulation, the equivalent circuit modeling techniques are preferred here considering their simplicity and light computational complexity 79, 80. We note that similar work has been reported in Ref. 81 for fuel cells and Ref. 24 for VRFBs. As depicted in Fig. 4c, the equivalent circuit is composed of a series of flow resistances, such as $R_{ch}/(\theta - 1)$ for each channel segment and R_{ele}/θ for each electrode segment. Here, R_{ch} corresponds to the flow resistance associated with a single channel flowing in the x direction, which can be estimated through the Darcy-Weisbach equation 82:

$$R_{ch} = \frac{128\mu L}{\pi D_h^4}, \quad (58)$$

with D_h being the hydraulic diameter of the rectangular channel defined as follows 83:

$$D_h = \frac{2H_{ch}w_{ch}}{H_{ch} + w_{ch}}. \quad (59)$$

The term R_{ele} indicates the flow resistance associated with the electrode under rib flowing in the y direction, estimated by the Darcy's law [83]:

$$R_{ele} = \frac{\mu w_{rib}}{\kappa H_e L}. \quad (60)$$

The pressure at the entrance of the outlet channel, p^* , can be analytically expressed as a function of p_{in} , R_{ch} , and R_{ele} by imposing basic circuit rules (i.e., Kirchhoff's circuit laws [84]). We note that this expression increases in reliability with larger values of θ ; however, our numerical investigation on the change of p^*/p_{in} with respect to θ revealed that $\theta = 2$ can provide the simplest expression with acceptable errors ($< 5\%$). This expression is given as follows:

$$\frac{p^*}{p_{in}} \approx \frac{p^*}{p_{in}} \Big|_{\theta=2} = \frac{R_{ch}}{2R_{ele} + R_{ch}}. \quad (61)$$

Our further investigation showed that the pressure distribution along an outlet channel in x direction (i.e., $p(x)$) can be well approximated by a half parabola that has axis of symmetry on the entrance side. Knowing the approximated analytical expression of $p(x)$, it is easy to find the value of \bar{p}_{out}/p^* as follows:

$$\frac{\bar{p}_{out}}{p^*} \approx \frac{\frac{1}{L} \int_0^L p(x) dx}{p^*} \approx \frac{2}{3}. \quad (62)$$

This results in an analytical expression of \bar{p}_{out} as a function of p_{in} by combining Eqs. (61) and (62) as follows:

$$\bar{p}_{out} \approx \frac{2}{3} \cdot \frac{R_{ch}}{2R_{ele} + R_{ch}} p_{in}. \quad (63)$$

The detailed derivation can be found in Section S1 of the Supporting Information.

Hereafter, with the assumption of imposed zero pressure at the outlet, the inlet pressure (i.e., p_{in}) for IDFF can be estimated by an empirical equation [78, 85]:

$$p_{in} = \frac{8\mu QL (w_{ch} + H_{ch})^2}{N w_{ch}^3 H_{ch}^3} \left(1 + \frac{2 + 2 \cosh \xi}{\xi \sinh \xi} \right), \quad (64)$$

where N is the number of channels ($N = 7$ here, following the configuration given in [86]), w_{ch} , w_{rib} , H_e , H_{ch} , and L are the geometric quantities as shown in Fig. 2. The quantity ξ is given as follows:

$$\xi^2 = \frac{32L^2 \kappa H_e (w_{ch} + H_{ch})^2}{(w_{ch} + w_{rib} + H_e) w_{ch}^3 H_{ch}^3}. \quad (65)$$

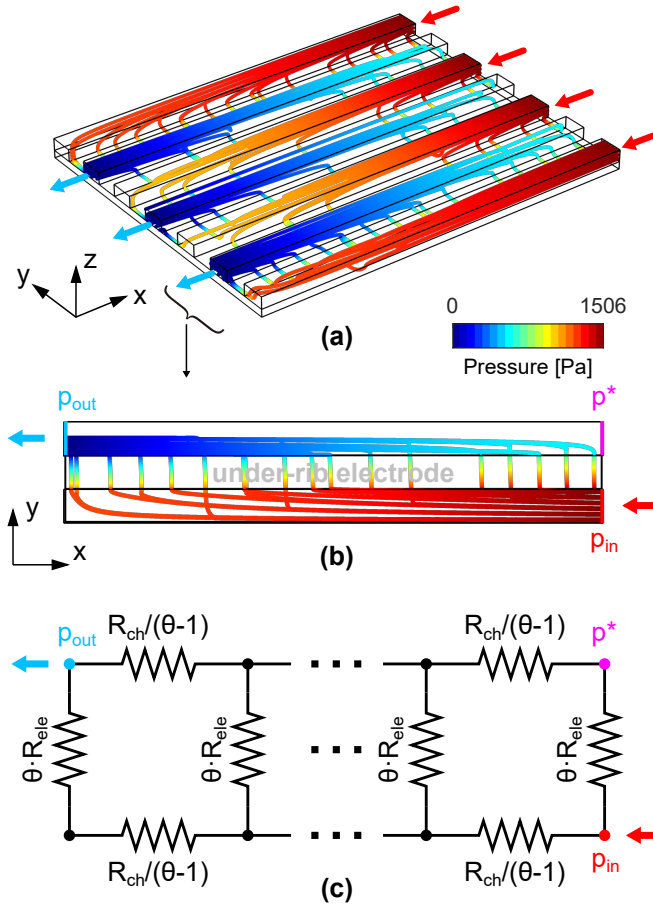


Figure 4: (a) 3D view of the streamlines indicating how the electrolyte flows from inlets to outlets for IDFF (negative half-cell) at 10 mL min^{-1} , obtained from the 3D simulation, (b) emphasized top view of the streamlines indicating how the electrolyte flow from one inlet to an adjacent outlet, (c) an equivalent electrical circuit to simulate the pressure distribution in (b). θ represents the number of segments for the electrode portion. $R_{ch}/(\theta - 1)$ and $\theta \cdot R_{ele}$ refer to flow resistance for each channel and electrode segment, respectively.

3. Experiment

3.1. Materials and methods

Sulfuric acid (95.0–98.0%, Sigma-Aldrich) and vanadium (IV) sulfate oxide hydrate (99.9%, Alfa Aesar) were used as received to create the electrolyte for the full VRFB cell. All experimental reagents were prepared and stored at room temperature.

3.2. Experimental setup

3.2.1. Vanadium redox flow cell

Two untreated Freudenberg H23 (Fuel Cell Store) electrodes were cut with a razor to $1.4\text{ cm} \times 1.6\text{ cm}$ yielding a ca. 2.24 cm^2 geometric area that were stacked on each side of the cell. The electrode compression was controlled with polytetrafluoroethylene gaskets to ca. $(20 \pm 2)\%$ of the measured thickness ($\pm 15\text{ }\mu\text{m}$, Mitutoyo 7326S caliper). To prepare the electrolyte for polarization, 50 mL of 1.5 M VO_2^+ and 2.6 M H_2SO_4 were each placed in two glass reservoirs under a humidified nitrogen sparge. An Easy-Load II peristaltic pump (Cole-Parmer) with Masterflex L/S 16 tubing pumped the electrolyte at 10 mL min^{-1} from the reservoirs to the positive and the negative sides of the flow cell. The electrolyte was forced through an IDFF before contacting the electrodes and the Nafion 212 membrane (Fuel Cell Store; used as received). The electrolyte then exits the reactor body and returns to the reservoirs. A schematic of the cell is shown in Fig. 5a. All electrolytes for this study were pumped through the cell for 50 min to promote wetting and to remove trapped air bubbles. An Arbin Battery Tester (FBTS, Arbin Instruments) was used to convert the two VO^{2+} electrolytes to VO_2^+ on the positive side and V^{2+} on the negative side by holding a 1.7 V potential until ca. 0 A was measured. The VO_2^+ electrolyte was discarded and replaced with the identical VO^{2+} solution as described (*vide supra*). Prior to polarization, a new VRFB assembly was used to achieve a 50 % SOC by first charging the cell to 100 % SOC (1.7 V) at 255 mA and then to 0 % SOC (0.9 V) with -255 mA . Immediately following, the cell was charged at 255 mA for half the discharge time to achieve a 50 % SOC. The polarization was then performed with constant 25.5 mA discharge increments for 2 min, after which a 25.5 mA charging current density was used to restore the system to 50 % SOC. The polarization procedure was conducted from OCV to 0.7 V. The last 10 data points for the discharge current steps were averaged to generate the polarization curve.

3.2.2. Electrochemical double-layer capacitance

The electrochemical double-layer capacitance (EDLC) experiment was performed to estimate the surface area of the two-electrode stacks in the flow cell. A ca. 20 mL 2.6 M H_2SO_4 solution was used to measure the average non-Faradaic currents as calculated by:

$$I_{EDLC} = \frac{1}{2} (I_{ox} + |I_{red}|), \quad (66)$$

where I_{EDLC} is the EDLC-measured current, I_{ox} is the oxidative current, and I_{red} is the reductive current. The single electrolyte configuration [87] was used to determine the EDLC as shown in

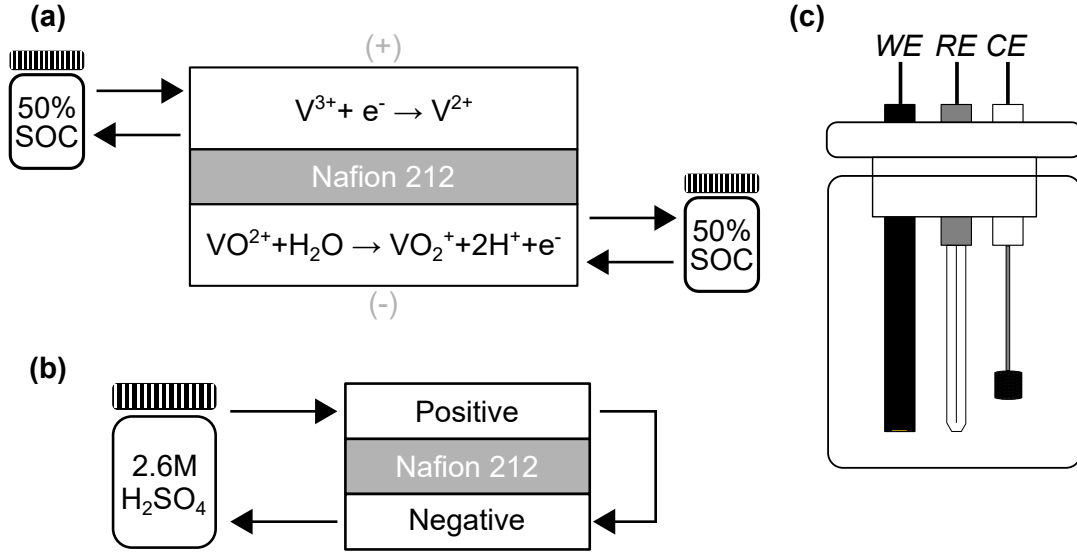


Figure 5: (a) The VRFB schematic showing the 50 % SOC for both the positive and the negative sides, (b) the single electrolyte configuration for measuring the EDLC with the H_2SO_4 supporting salt, (c) the three-electrode set-up with the glass carbon working electrode (WE), the Ag/AgCl reference electrode (RE) and the Pt mesh counter electrode (CE)

Fig. 5b, where the electrolyte is drawn at 10 mL min^{-1} from the reservoir to the positive side, then immediately passed through the negative side before returning to the reservoir. After a 20 min flow to promote wetting, cyclic voltammograms (CVs) were taken with a Bio-Logic VMP-3 at scan rates of 50, 100, 200, 300, and 400 mV s^{-1} with 100 % resistance compensation. The I_{ox} and the I_{red} values were estimated from the current values closest to 0 V to determine I_{EDLC} ; this experiment was repeated once. After testing, the electrodes were removed and the same CV scan rates were used to determine and to subsequently subtract off the non-Faradaic currents from a blank cell. The slope of I_{EDLC} vs. the scan rate (\dot{v}) was used to determine the electrode capacitance (C_e), as shown in Eq. (67):

$$\frac{dI_{EDLC}}{d\dot{v}} = C_e. \quad (67)$$

Using C_e , the estimated electrode specific surface area per mass (A_M) can be calculated through:

$$A_M = \frac{C_e}{\tilde{C}_{ref} m_e}, \quad (68)$$

where \tilde{C}_{ref} is the capacitance of a model surface and m_e is the mass of the electrode. The model surface capacitance can be measured through a three-electrode set-up (Fig. 5f) using a material with a known surface area. A 3 mm diameter glass carbon (CH Instruments) electrode was used as the working electrode in conjunction with a Ag/AgCl reference electrode (CH Instruments), and an in-house Pt mesh counter electrode. The glassy carbon electrode was polished with a 0.05 μm alumina slurry MicroPolish on a MicroCloth polishing cloth (Buehler), before drying with de-ionized water and lens paper (VWR). CVs were taken in the three-electrode configuration with ca. 20 mL 2.6 M H_2SO_4 solution in a glass scintillation at scan rates previously described (*vide supra*) using a Bio-Logic VSP with 100% resistance compensation. This measurement was repeated once, and the calculations for determining \tilde{C}_{ref} are identical to those described in Eqs. (66) and (67).

4. Models calibration and validation

4.1. Numerical solution

The developed physical models presented in this paper are solved using COMSOL Multiphysics[®] modules [88]. COMSOL Multiphysics[®] is a user-friendly computational platform for computing coupled multiphysics-based problems. While there are limited innate solver types, COMSOL Multiphysics[®] has flexible equation modifications and implementation, which are paramount for this study. The weak form of the governing equations is discretized in space by standard Galerkin Finite Element (FE) method. The three-node triangle elements in 2D and four-node tetrahedral elements in 3D are used to approximate the state variables. To prevent numerical instabilities and oscillations in the solutions of the incompressible Navier-Stokes and advection-diffusion equations [89, 90], the weak forms of the governing equations are affixed with consistent stabilization terms corresponding to streamline-diffusion [91] and crosswind-diffusion [92].

A global mesh refinement with 1.06×10^7 elements is used to discretize the 3D model, where a mesh refinement based on a local solution is used to increase the accuracy of the fluid dynamic responses with 2.11×10^7 elements. The 2D model is discretized with 2.11×10^4 elements. The meshes are generated using COMSOL built-in unstructured mesh generation methods, which show higher flexibility when applied to a complex geometry compared to the structured ones [93]. Finer elements are prescribed in the sharp corners, boundaries, etc., to capture the possible steep variations. More details can be found in Section S2 of the Supporting Information, such as a mesh

refinement study showing negligible discretization errors. For the results presented in this study sufficiently fine meshes with negligible errors are considered. An iterative Algebraic Multigrid method [94] is used to solve 3D equations and a direct linear solver is used to solve 2D formulations. The discretized nonlinear problem is considered to converge if the norm of the Newton update step is less than the relative tolerance of 1×10^{-4} .

All numerical simulations are performed in a Linux environment with Intel® Core™ i5-8500 (Hexa-Core, 3.00 GHz) processor and random-access memory (RAM) of 32 GB. The detailed comparison of consumed computational resources for each polarization point between the two different models are listed in Table 2.

Table 2: Comparison of consumed computational resources averaged for each polarization point between 3D and 2D models. The data are recorded for U_{cell} from 0.1 V to 1.349 V.

Case	Memory usage	Average simulation duration
3D	30.89 GB	2137.87 s per point
2D	4.72 GB	9.96 s per point

4.2. Model parameters

Herein, we present material and model parameters used in the numerical simulation. In the cases where the experimental methods were not feasible, numerical fitting is used to determine the parameters and the extracted values are compared to the peer-reviewed literature. Unless otherwise stated, all model and material parameters are listed in Tables 3-5 with references for the parameters given in the Ref. column, where the abbreviations exp., mfr., and est. refer to experiment, manufacturer, and estimated, respectively.

The Carman-Kozeny constant, k_{CK} , is estimated by fitting the experimentally measured permeability with the same compressed porosity, as previously reported in Ref. [96]. The porosity, ε , is determined using an electrode mass equation defined as:

$$\varepsilon = 1 - \frac{H'_e}{H_e} (1 - \varepsilon'), \quad (69)$$

where H'_e and ε' are the uncompressed electrode thickness and porosity, respectively. The value of ε' is reported as 0.74 from mercury intrusion porosimetry [95]; whereas, the value of H'_e is directly measured and listed in Table 5.

Table 3: Model parameters and properties used in numerical simulations. The abbreviations exp. and mfr. refer to experiment and manufacturer, respectively.

Symb.	Description	Value	Ref.
\mathcal{R}	Universal gas constant	$8.3145 \text{ J mol}^{-1} \text{ K}^{-1}$	
\mathcal{F}	Faraday constant	$96\,485.3329 \text{ A s mol}^{-1}$	
A_V	Volumetric area	$238\,301 \text{ m}^2 \text{ m}^{-3}$	exp.
ε	Compressed porosity	0.68	exp.
d_f	Mean fiber diameter	$9 \mu\text{m}$	[95]
k_{CK}	Carman-Kozeny constant	0.42	[96]
ρ_-	Negative electrolyte density	$1338.06 \text{ kg m}^{-3}$	exp.
ρ_+	Positive electrolyte density	$1357.20 \text{ kg m}^{-3}$	exp.
μ_-	Negative electrolyte viscosity	$5.423 \times 10^{-3} \text{ Pa s}$	[97]
μ_+	Positive electrolyte viscosity	$4.827 \times 10^{-3} \text{ Pa s}$	[97]
β	Degree of dissociation for HSO_4^-	0.25	[50]
k_d	Dissociation rate constant for HSO_4^-	$1 \times 10^4 \text{ mol m}^{-3} \text{ s}^{-1}$	[50]
D_{H}	Diffusivity of H^+	$9.312 \times 10^{-9} \text{ m}^2 \text{ s}^{-1}$	[61]
D_{HSO_4}	Diffusivity of HSO_4^-	$1.330 \times 10^{-9} \text{ m}^2 \text{ s}^{-1}$	[61]
D_{SO_4}	Diffusivity of SO_4^{2-}	$1.065 \times 10^{-9} \text{ m}^2 \text{ s}^{-1}$	[61]
$D_{\text{V}2}, D_{\text{V}3}$	Diffusivity of V^{2+} and V^{3+}	$1.300 \times 10^{-10} \text{ m}^2 \text{ s}^{-1}$	[98]
$D_{\text{V}4}, D_{\text{V}5}$	Diffusivity of VO^{2+} and VO_2^+	$7.740 \times 10^{-11} \text{ m}^2 \text{ s}^{-1}$	[98]
$\alpha_{a,t}, \alpha_{c,t}$	Anodic and cathodic charge transfer coeff.	0.5	[49]
$E_{0,-}$	Negative standard equilibrium potential	-0.255 V	[61]
$E_{0,+}$	Positive standard equilibrium potential	1.004 V	[61]
k_-	Negative standard rate constant	$3.3 \times 10^{-8} \text{ m s}^{-1}$	fitted
k_+	Positive standard rate constant	$6.8 \times 10^{-7} \text{ m s}^{-1}$	[99]
T	Temperature	295 K	exp.
$\sigma_{s,e}$	Electronic conductivity of electrode	377.78 S m^{-1}	mfr.
$\sigma_{l,mem}$	Ionic conductivity of membrane	1.04 S m^{-1}	fitted
a	Parameter for $k_m = b \mathbf{u} ^a$	0.4	[73]
b	Parameter for $k_m = b \mathbf{u} ^a$	1.33×10^{-5}	fitted

Table 4: Initial concentrations at 50% SOC. The abbreviations exp. and est. refer to experiment and estimated, respectively.

Symb.	Description	Value	Ref.
$c_{V_2}^0$	Initial concentration of V^{2+}	750 mol m^{-3}	exp.
$c_{V_3}^0$	Initial concentration of V^{3+}	750 mol m^{-3}	exp.
$c_{V_4}^0$	Initial concentration of VO^{2+}	750 mol m^{-3}	exp.
$c_{V_5}^0$	Initial concentration of VO_2^+	750 mol m^{-3}	exp.
$c_{H,+}^0$	Initial concentration of H^+ (positive)	$3718.75 \text{ mol m}^{-3}$	est.
$c_{H,-}^0$	Initial concentration of H^+ (negative)	$2781.25 \text{ mol m}^{-3}$	est.
$c_{HSO_4,+}^0$	Initial concentration of HSO_4^- (positive)	$2231.25 \text{ mol m}^{-3}$	est.
$c_{HSO_4,-}^0$	Initial concentration of HSO_4^- (negative)	$1668.75 \text{ mol m}^{-3}$	est.
$c_{H,+}^{ini}$	H^+ concentration at SOC = 0 (positive)	5200 mol m^{-3}	est.
$c_{H,-}^{ini}$	H^+ concentration at SOC = 0 (negative)	3700 mol m^{-3}	est.

The positive standard rate constant, k_+ , the ionic conductivity of the membrane, $\sigma_{l,mem}$, and the empirical constant for the mass transfer coefficient, b , are determined by the numerical curve fitting of the simulated and experimental polarization curves. The residuals of the curve fitting are shown in Fig. S11 in the Supporting Information:

- The positive standard rate constant, k_+ , is set to $6.8 \times 10^{-7} \text{ m s}^{-1}$. The value is adopted from the experimental results given in [99]. However, the negative standard rate constant, k_- is numerically fitted to $3.3 \times 10^{-8} \text{ m s}^{-1}$. These values are in agreement with the previously reported numerical [10, 49-51, 54, 57, 100-106] and experimental [107] studies.
- The ionic conductivity of the Nafion 212 membrane, $\sigma_{l,mem}$, is numerically fitted to 1.04 S m^{-1} . We note that this quantity varies from the experimentally-determined value of 5.4 S m^{-1} [108] but is in agreement with previously reported studies [109], which has been hypothesized to be the result of variations in contact resistance. We note that this quantity varies from the experimentally-determined value of 5.4 S m^{-1} [108] but is in agreement with previously reported studies [109], which has been hypothesized to be the result of variations in contact resistance. While there is evidence that membrane thickness, H_{mem} , can enlarge due to

Table 5: Geometric parameters of the VRFB model. The abbreviations exp. and mfr. refer to experiment and manufacturer, respectively. The configuration is the same as previous work [86].

Symb.	Description	Value	Ref.
L	Length of the electrode	16 mm	exp.
W	Width of the electrode	13 mm	exp.
w_{ch}	Channel width	1 mm	exp.
w_{rib}	Rib width	1 mm	exp.
H_{ch}	Channel thickness	0.5 mm	exp.
$H_{e,-}$	Negative electrode thickness	3.1496×10^{-4} m	exp.
$H_{e,+}$	Positive electrode thickness	3.0988×10^{-4} m	exp.
$H'_{e,-}$	Pristine negative electrode thickness	3.9624×10^{-4} m	exp.
$H'_{e,+}$	Pristine positive electrode thickness	3.9624×10^{-4} m	exp.
H_{mem}	Membrane thickness	50.8 μ m	mfr.

swelling [110, 111], H_{mem} does not influence the fluid dynamics, and the electrochemical changes would be captured by fitting the $\sigma_{l,mem}$ to the experimental data.

- The empirical constant a is set to 0.4 and the other constant b is numerically fitted to 1.33×10^{-5} . According to previous work [112, 113], the exponent constant a is typically in the range of 0.3 to 0.5 for laminar flow. This value of a (i.e., 0.4) is also widely reported in previous modeling studies [14, 40, 49, 54–57, 114–119]. For b , the fitted value, 1.33×10^{-5} , is within the range of the previously reported values; for example, $k_{m,-} = 1.69 \times 10^{-5} |\mathbf{u}|^{0.4}$ and $k_{m,+} = 1.07 \times 10^{-5} |\mathbf{u}|^{0.4}$ as reported in Delanghe et al. [120].

4.3. Models validation

Here, the validation of the developed VRFB models against the experimental results is described. In particular, the performance of the 3D is compared against the experimental polarization curve at a flow rate of 10 mL min^{-1} and from OCV to 0.627 V, as detailed in Section 3. The discharge polarization curve generated in this study is similar to previous work [96] with a comparison of the experimental and the simulated polarization curves is shown in Fig. 6 revealing that the 3D simulation is in excellent agreement with the experimental data. The mean relative error (MRE) and

root-mean-square error (RMSE) of the 3D simulated results with respect to the experimental ones are 0.32 % and 5.4 mV. The RMSE, frequently used as a measure for the deviation between model predicted and experimental data, is calculated as the square root of the mean square of the fitting residuals [121, 122]. It (5.4 mV) is negligible compared to the U_{cell} range of approximately 0.6–1.4 V, suggesting an excellent fit [122, 123]. The largest discrepancy of ca. 2.5 % is observed near the zero current density, which could be caused by the difference between the predicted (i.e., Eqs. (17) and (18)) and experimental OCV [70]. This discrepancy can be attributed to the assumption of unit activity coefficients, according to previous work [70]. Similar discrepancies have also been reported of $\pm 1.2\%$ ([70]) and 1.9–2.8% ([124]), demanding further work on improving the OCV prediction precision. Additionally, the polarization curve generated from the 2D and the 3D models are compared. Considering that one of the main goals of this work is to establish a methodology for simplifying a computationally-expensive 3D model with interdigitated flow fields into a light 2D model, while retaining accuracy, we extend the comparison range from OCV–0.627 V to OCV–0.1 V to cover the high current density region that is dominated by the mass transfer losses [109]. We acknowledge that the experimental data does not extend to the 0.1 V; however, this abbreviated experimental range can still be used for model validation and subsequent analysis [41, 42, 44, 102, 118, 125–127]. The comparison between the two models shows good agreement across the entire current density region with MRE and RMSE of 0.43 % and 3.8 mV, respectively. The greatest relative difference between two simulations remains less than 0.5%. It can be seen that the 2D model provides an accurate polarization behavior with largely reduced computational cost.

We further investigated the performance of the 2D model by comparing the spatial variations of the cell responses with the corresponding 3D ones. The comparison of the fluid dynamic responses (i.e., velocity yz component and pressure) is shown in Fig. 7a and b, and the comparison of the electrochemical responses (i.e., vanadium concentration, electric potential in both liquid and solid phases, and overpotential) at 0.1 V are presented in Fig. 7c-f. The electrochemical responses at 0.5, 0.9, and 1.3 V are also examined and presented as Fig. S12-S14 of the Supporting Information. The second column of the figures is the x -averaged 3D responses, computed as follows:

$$\bar{(\cdot)} = \frac{1}{L} \int (\cdot) dx,$$

where (\cdot) is the corresponding 3D response. From the comparison of the first and second columns in Fig. 7, the 2D responses show good agreement with the averaged 3D values for both fluid dynamic

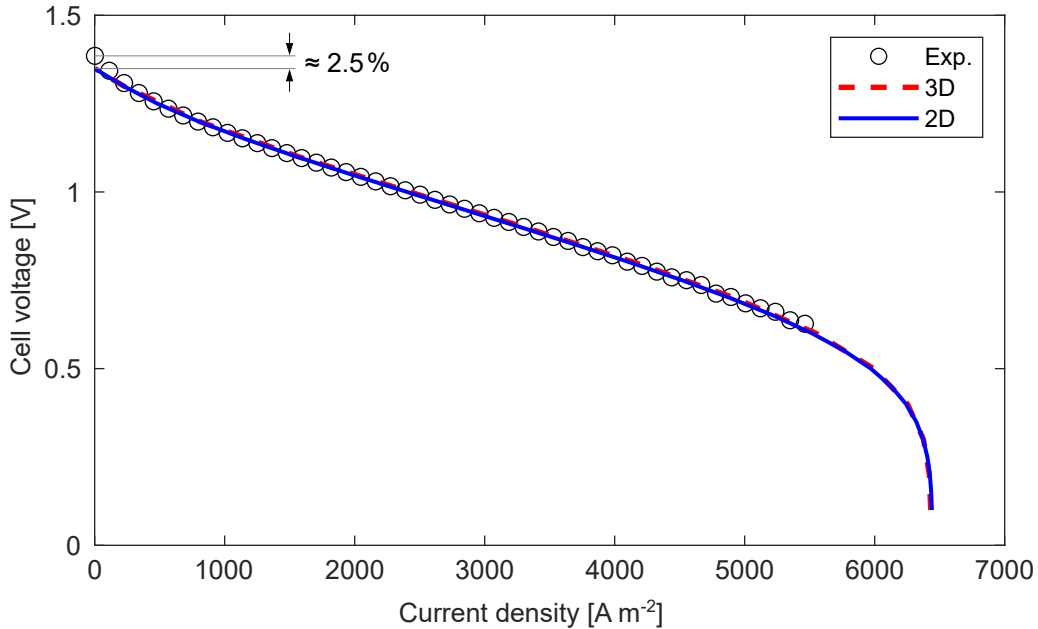


Figure 6: Comparison of polarization curves of the 3D and 2D simulations and the experimental data. “Exp.” refers to experiment.

and electrochemical quantities. As shown in Fig. 7a, c-e, the largest discrepancies occur at the region near the outlet. For the 2D velocity and concentration responses, it can be seen that overshoots exist at the inlet and/or outlet boundaries. This can be caused by the approximated 2D inlet and outlet boundary conditions assumed at the interfaces between the channel and flow field (Eqs. (42) and (53)). However, in reality, these boundaries are enclosed partial walls. Furthermore, there are small discrepancies in the pressure distribution at the outlet and the intermediate inlet channels that come from the estimation of x -averaged outlet pressure (Eqs. (63) and (64)). This estimation assumes that the pressure at all the inlet boundaries are equal; but, as shown in the 3D result, the intermediate inlets have a lower pressure than the outer inlets. Nevertheless, the 2D model provides a reasonable pressure drop prediction, though an accurate pressure distribution might be difficult to obtain with a planar 2D model. We note that our 2D model shows good agreement on the fluid dynamic responses with respect to the 3D model for different flow rates ($1\text{--}15\text{ mL min}^{-1}$), as presented in Fig. S15-S17 in the Supporting Information. These comparisons demonstrate that incorporating the x -averaged outlet pressure retains the fluid dynamic accuracy of the 2D model.

Additionally, a simple scale-up study on the \bar{p}_{out} estimation (Eq. (63)) is performed to check its ability to scale to larger cells. The study shows that Eq. (63), which is obtained from $\theta = 2$, works well only when the channel length within a limited range (i.e., approximately 0–2 cm), while better performance across the entire channel length range can be achieved by increasing the value of θ . The results are attached in Section S5 of Supporting Information. We note that evaluating the performance of the 2D modeling framework for other flow fields—such as SFF and PFF—are beyond the scope of this paper. However, some of the assumptions considered in this paper only hold for IDFF, hence additional examinations might be necessary for other flow field configurations.

5. Results and discussion

We describe the results of the extensive parametric analysis of the negative electrode to show trends in the overall cell current density for different cell voltages during discharge. We first justify the cell-level and electrode parameters used in this study and define a structural dimensionless number composed of different parametric input variables to aid in visualization of the electrode design space. We then discuss the electrochemical and the hydrodynamic performance from the parametric sweep. Finally, we quantify the correlations in various structural parameters with the electrochemical and fluid dynamic performance of the cell and posit an improved electrode structure.

5.1. Parametric Sweep Selection

The parametric analysis was performed by altering the physical input values for the negative electrode in the 2D model. The negative electrode was chosen to study the isolated effect of macro-homogeneous electrode structure on cell performance since it typically has the slower reaction kinetics [128]. Additionally, while other cell-level parameters—such as flow rate [60] and concentrations [50]—could be adjusted (and often are in practice to improve performance), we chose to only modify the structural properties to later demonstrate possible single electrode improvements in the electrochemical and fluid dynamic performance. In particular, the structural parameters are $H_{e,-}$, ε_- , $d_{f,-}$, $A_{V,-}$, and k_- for six full-cell polarization voltages. We selected these parameters without presupposition of interrelations in order to observe far-reaching possible various electrode morphologies. However, the parameter sweep values herein are not unrealistic, as various peer-reviewed literature observe the electrode properties as shown in Table 6 for $H_{e,-}$ [129, 130], ε_- [95], $d_{f,-}$ (κ_-) [131], $A_{V,-}$ [21], and k_- (*vide supra*).

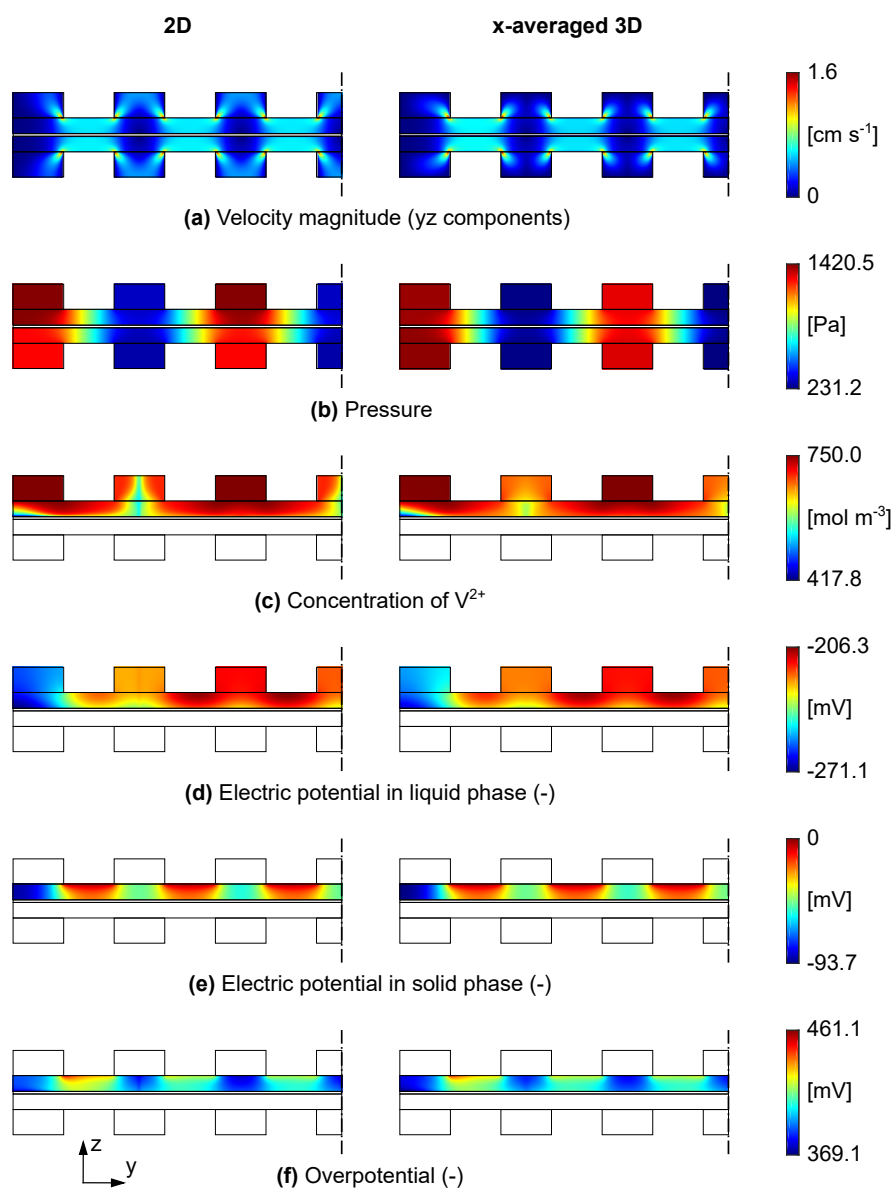


Figure 7: Comparison of the fluid dynamic and electrochemical responses between the 2D and 3D simulations at 10 mL min^{-1} and 0.1 V : (a) velocity magnitude (yz components), (b) pressure, (c) concentration of V^{2+} , (d) liquid-phase electric potential, (e) solid-phase electric potential, and (f) overpotential. In (c-f), only the negative half is shown.

Importantly, $d_{f,-}$, which is only used in estimating permeability through the Carman-Kozeny equation (Eq. (6)), has no relationship with the current density as there is no direct connection between the two variables within the set of fundamental physical equations. Additionally, the permeability varies in all spatial directions and is a function of the microstructural properties of the system, which is commonly estimated through the Carman-Kozeny equation (Eq. (6)), and, more specifically, the k_{CK} and d_f . Instead of using the 3D tensor and k_{CK} values for each direction, the bulk averaged permeability, corresponding to different $d_{f,-}$ and constant k_{CK} through all directions, was implemented, primarily to treat the electrode as macrohomogeneous. Indirectly, the permeability value in these simulations, derived from $d_{f,-}$, contains information regarding the porous media but is not manifested in the output current density. A direct sensitivity analysis of the structure would need to include information such as the tortuosity and the pore size distribution not captured in this simulation domain, largely due to computational expense. Nevertheless, this bulk scalar quantity can be used in lieu of more detailed information in order to determine the sensitivities of other parameters on the electrochemical response of the system.

Similarly, the $A_{V,-}$ quantity was directly input instead of employing an approximation. Previous models typically use A_V estimations, such as the long-fiber approximation [43, 59, 60]. However, previous work has shown that the long-fiber approximation can differ from *in situ* EDLC measurements by more than an order of magnitude [132]. Indeed, using the long-fiber approximation would reveal electrochemical trends by varying the $d_{f,-}$, but given the variety of surface area [133] approximation and the lack of *in situ* estimations for RFBs, we chose to keep the $A_{V,-}$ quantities unconstrained.

This parametric analysis results in 44 100 different simulation results. To aid in the visualization of the data, a dimensionless quantity was introduced to define a unique variable that is a function of input parameters. Often, this non-dimensionalization can aid in combining multiple simulation inputs into a single quantity [43, 59, 60]. The dimensionless quantity is defined as follows:

$$\Pi\text{-Group} = H_{e,-} \cdot \varepsilon_-^{-1} \cdot A_{V,-}. \quad (70)$$

5.2. Polarization and pressure drop trends

To assess the effect of the negative electrode structural components on the electrochemical performance, $i \cdot i_0^{-1}$ is plotted against the structural parameters at 1.3, 1.1, 0.9, 0.7, 0.5, and 0.3 V

Table 6: Parameter list for the parametric analysis.

Parameters	Unit	Values	Count
$H_{e,-}$	10^{-4} m	1, 3, 5, 7, 10, 15, 20	7
ε_-	–	0.60, 0.65, 0.70, 0.75, 0.80, 0.85, 0.90	7
$d_{f,-}$	10^{-6} m	5, 6, 7, 8, 9	5
$A_{V,-}$	10^5 m ² m ⁻³	0.1, 1, 1.9, 2.8, 3.7, 4.6	6
k_-	10^{-7} ms ⁻¹	0.2, 0.7, 1.2, 1.7, 2.2	5
U_{cell}	V	0.3, 0.5, 0.7, 0.9, 1.1, 1.3	6

for Fig. 8a, b, c, d, e, and f, respectively, with the color of the points referring to the different k_- values. Indeed, there is a large operation space for the polarization as the myriad of combinations of $H_{e,-}$, ε_- , and $A_{V,-}$ can yield regions of high and low performance. For all cell voltages, the effect of k_- aligns with intuition: as the reaction rate increases, i_0 increases and thus the $i \cdot i_0^{-1}$ quantity decreases. Additionally, as the cell continues to discharge at lower cell voltages, the value of i increases. Interestingly, the dimensionless parameter spans multiple orders of magnitude (Fig. 8) and reveals several regions of improved current density. However, as the cell voltage reaches mass transfer limiting regimes, the changes in the structural properties do not evince improvements in the current density. This phenomena is can be seen in Fig. 8e and f at $H_{e,-} \cdot \varepsilon_-^{-1} \cdot A_{V,-}$ values above 100.

The fluid dynamic response of the macrohomogeneous modifications can also be considered primarily through the changes in the pressure drop along the electrode, i.e., Δp_- . However, as shown in Eqs. (4) and (5), there are no direct relationships between $A_{V,-}$, U_{cell} , and k_- with the fluid dynamics. As such, only the modifications in $H_{e,-}$, ε_- , and $d_{f,-}$ are used for comparative metrics of the pressure drop.

The variation of pressure drop with respect to these three parameters are presented as Fig. 9 where all the quantities except $d_{f,-}$ are non-dimensionalized to facilitate scaling [62, 134]. The non-dimensional pressure drop is defined as the Bejan number (Be) [135, 136]:

$$\text{Be} = \frac{\Delta p_- L^2}{\mu_- \nu_-}, \quad (71)$$

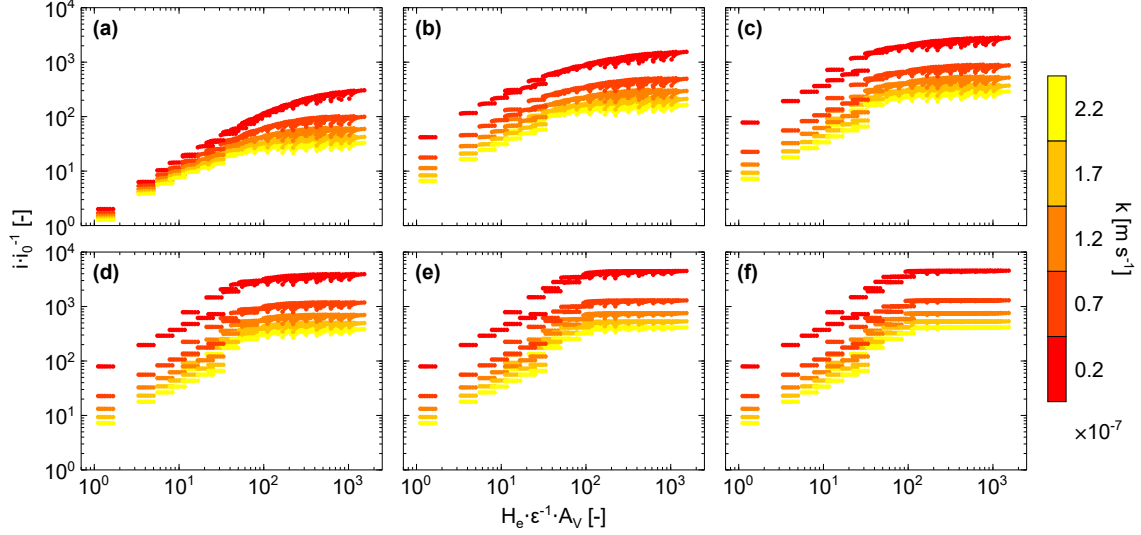


Figure 8: The responses in the $i \cdot i_0^{-1}$ for different dimensionless quantity, $H_{e,-} \cdot \varepsilon_-^{-1} \cdot A_{V,-}$, for different k_- values at (a) 1.3 V, (b) 1.1 V, (c) 0.9 V, (d) 0.7 V, (e) 0.5 V, and (f) 0.3 V. The subscript “-” representing negative half-cell is neglected in the figure.

where ν is the kinematic viscosity defined as

$$\nu_- = \frac{\mu_-}{\rho_-},$$

and L (i.e., flow field channel length) is the characteristic flow length of the VRFB with IDFF [85]. Furthermore, the $H_{e,-}$ is non-dimensionalized as $H_{e,-} W^{-1}$. The porosity (ε_-) is already a non-dimensional quantity, and the $d_{f,-}$ is left with dimensions.

Fig. 9a, b, and c show the Be as function of the $d_{f,-}$ and the ε_- for respective $H_{e,-}$ values of 1×10^{-4} , 7×10^{-4} and 20×10^{-4} m; and, Fig. 9d, e, and f show the Be as function of the $d_{f,-}$ and the $H_{e,-}$ for respective ε_- values of 0.60, 0.75, and 0.90. For Fig. 9a-c, decreasing $d_{f,-}$ results in increases in Be due to the relationship with Carman-Kozeny equation. The effect of $H_{e,-}$ can also be seen, as at higher values of $H_{e,-}$ the values of Be decreases. This can also be seen in Fig. 9d-f, where increases in $H_{e,-} \cdot W^{-1}$ reveal lower Be. The effect of the change in ε_- show nearly indistinguishable plots, suggesting the system is more sensitive to changes in $H_{e,-}$ and $d_{f,-}$ for influencing the overall fluid dynamics. Holistically, these plots depict a region of high and low pressure loss across the cell that arises from the variations of the intraelectrode velocities; plots of the corresponding Reynolds number are shown in Fig. S19 and S20 of the Supporting Information

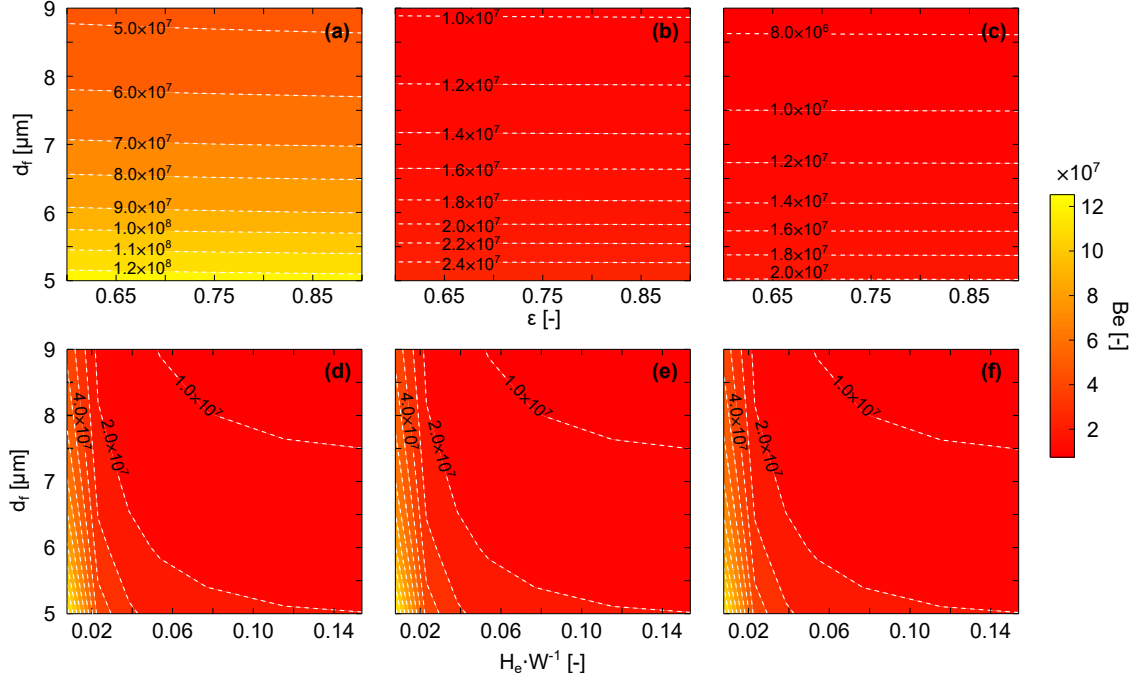


Figure 9: The Be as function of the $d_{f,-}$ and the ε for respective $H_{e,-}$ values of (a) 1×10^{-4} , (b) 7×10^{-4} , and (c) 20×10^{-4} m. Additionally, the Be as function of the $d_{f,-}$ and the $H_{e,-}$ for respective ε values of (d) 0.60, (e) 0.75, and (f) 0.90. The subscript “-” referring to negative electrode is neglected in the figure.

to show the changes at different electrode thicknesses, porosities, and fiber diameters.

5.3. Quantitative calculations

Hitherto, trends in simulation data have been qualitatively discussed and the effect of different parameters on electrochemical and fluid dynamics have been explored. However, large data set affords the ability to identify quantitative relationships between various input and output parameters through correlation analyses. The Kendall τ rank correlation coefficient [137] can be used to determine the correlations between the structural inputs and various electrochemical and fluid dynamic outputs. Unlike the Pearson correlation, the Kendall correlation is a robust calculation for non-linear data [138] with outliers [139]. The equation for the Kendall rank correlation coefficient is defined as [137]:

$$\tau = \frac{2}{n(n-1)} \sum_{i=1}^n \sum_{j=1}^n \text{sign}(x_i - x_j) \text{sign}(y_i - y_j), \quad (72)$$

where

$$\text{sign}(\cdot) = \begin{cases} 1 & \text{if } (\cdot) > 0 \\ 0 & \text{if } (\cdot) = 0, \\ -1 & \text{if } (\cdot) < 0 \end{cases}$$

with τ values of 1 and -1 indicating perfect positive and negative correlations, respectively.

The current density output can be correlated to the different input parameters at various voltages during cell discharge. Fig. 10a shows the changes in the correlation values for $H_{e,-}$, ε_- , $A_{V,-}$, and k_- with the numerical values provided in Table S1 in the Supporting Information. The $d_{f,-}$ term is expected to be insensitive to the electrochemical terms as there is no direct relationship with in the fundamental equations, nor do we employ empirical estimations between $d_{f,-}$ and other parameters, such as $A_{V,-}$. Interestingly, $A_{V,-}$ has the largest positive correlation for all cell voltages. However, as the cell discharges at 0.3 V, $A_{V,-}$ and ε_- suddenly decrease, while $H_{e,-}$ increases in correlative strength. This may be a result of the cell entering the mass transfer limiting regime of the VRFB and the relative importance of the parameters shifts.

Similar Kendall rank correlation calculations were performed for η_+ and η_- as shown in Fig. 10b and c with the respective numerical values shown in Table S2 and S3 in the Supporting Information. For η_+ , the $A_{V,-}$ increases in the correlative strength when the cell undergoes further polarization; whereas, k_- decreases in correlative value. The variations in τ for η_+ can largely be considered as responses to the changes in the η_- , as isolated negative electrode changes could only impact the η_+ through the cell resistance. Throughout discharge, $A_{V,-}$ has the largest magnitude value in the correlations, which can also be attributed to the dependence of surface area in promoting electrochemical reactions.

In evaluating τ for η_- , $H_{e,-}$ has near constant values across all cell voltages. Specifically, $H_{e,-}$ has a much stronger correlation with η_- than with η_+ , which is consistent with intuition as changes in $H_{e,-}$ would more significantly influence negative-side reactions since it modifies the domain for the electrochemical reactions. However, the ε_- has the smallest τ value indicating a weak correlation with η_- suggesting ε_- plays a minimal role in affecting η_- .

While the variations in $H_{e,-}$, ε_- , $A_{V,-}$, and k_- resulted in changes at each cell voltage, there is no relationship between the fluid dynamics and $A_{V,-}$, k_- , or U_{cell} . Thus, the Kendall τ rank correlation coefficient can be further applied to Δp_- and $k_{m,-}$ across all cell potentials as shown in Fig. 10d and e with the numerical values shown in Table S4 of the Supporting Information. For

Δp_- , all quantities have a negative τ value, which is consistent with the assumption of Brinkman flow. Both the $d_{f,-}$ and $H_{e,-}$ have the largest magnitude, indicating the greatest dependence on the pressure loss across the electrode. Interestingly, the $k_{m,-}$ exhibits a near unity negative relationship with $H_{e,-}$, indicating that the larger $H_{e,-}$ hinders the mass transfer in the overall cell performance do the effect a thicker electrode has on velocity scales within the electrode. ε_- has a slight negative correlation with $k_{m,-}$, while $d_{f,-}$ has a larger positive correlation.

Comparing the sign and the magnitude of the correlation coefficients, all of the input parameters can be adjusted to varying degrees to influence both i and Δp_- . Given this large data set representing a diverse array of electrode property profiles, an improved electrode that maximizes both electrochemical and fluid dynamic performance can be estimated. For the electrochemistry, the discharge power (P) for the flow cell can be determined as follows:

$$P = I \cdot U_{cell}, \quad (73)$$

where I denotes the current. To combine the electrochemical effects with the fluid dynamics, the pumping power as given in Eq. (74) can be calculated that includes both the positive and the negative pressure drop, where ψ_{pump} is the pump energy conversion factor that is typically assumed to be 0.9 [106].

$$\Xi = \frac{Q \cdot (\Delta p_- + \Delta p_+)}{\psi_{pump}}. \quad (74)$$

Ascribing equal weight to the discharge power and the pumping power, Eq. (73) and Eq. (74) can be combined to yield:

$$\zeta = \frac{P - \Xi}{P}, \quad (75)$$

where ζ is an objective function for the cell power efficiency representation. The maximum value of ζ reflects the combination of electrode configurations that achieves both high electrochemical power and low pressure loss; the value was determined to be $> 99\%$ yielding an improved electrode configuration of:

$$\left\{ \begin{array}{l} H_{e,-} = 1.5 \times 10^{-3} \text{ m}; \\ \varepsilon_- = 0.6; \\ A_{V,-} = 4.6 \times 10^5 \text{ m}^2 \text{ m}^{-3}; \\ k_- = 2.2 \times 10^{-7} \text{ m s}^{-1}; \\ d_{f,-} = 9.0 \times 10^{-6} \text{ m} \end{array} \right.$$

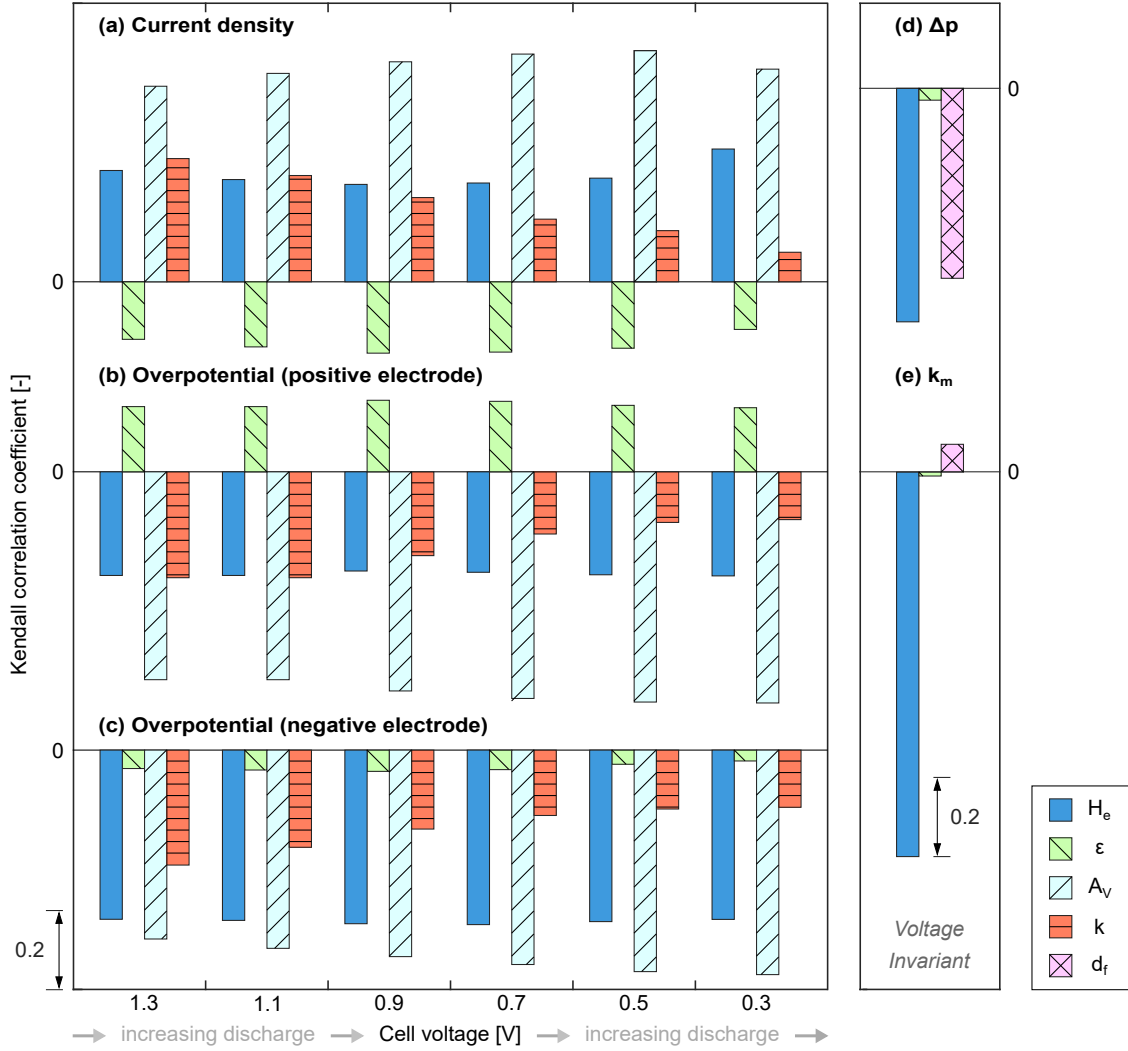


Figure 10: The Kendall rank correlations for the electrochemical response (left) of the $H_{e,-}$, ϵ_{-} , $A_{V,-}$, and k_{-} on (a) i , (b) η_{+} , and (c) η_{-} ; and the fluid dynamic response (right) of $H_{e,-}$, ϵ_{-} , and $d_{f,-}$ on (d) Δp_{-} and (e) $k_{m,-}$. The subscript “-” referring to negative electrode is neglected in the figure.

We note that this optimization procedure screens the available input data to the model, and thus the output is not a global optimization but rather a parameter search. However, the results of this procedure reveal that this improved electrode possesses the upper limit for $d_{f,-}$, $A_{V,-}$, and k_{-} and the lower limit for ϵ_{-} . This is due to the effect of $d_{f,-}$ solely acting to minimize the Δp_{-} across

the electrode and as $A_{V,-}$, k_- , ε_- working to maximize I , and thus P . However, as both $H_{e,-}$ and ε_- can impact both I and Δp_- , these simulations reveal that ε_- ignores the effect on minimizing Δp_- as $H_{e,-}$ is tuned for both electrochemical and fluid dynamic performance. This is observed in the Kendall τ values for Δp_- , as there was nearly no correlation between ε_- and Δp_- . Thus, in considering which parameters to adjust for an equal consideration of P and Ξ , $A_{V,-}$, k_- , and ε_- could solely be modified for the former, and $d_{f,-}$ for the latter with $H_{e,-}$ acting as an adjustable parameter for the trade-off between the the electrochemistry and the fluid dynamics.

The polarization curve of this improved electrode was compared to the experimental VRFB as shown in Fig. 11. The improved electrode exhibits a ca. 24% increase in power density as relative to the experimental assembly. We note that this improved electrode design considers the effects of Δp_- and is thus not the largest possible P . Additionally, the optimal value is limited by the range of swept parameters, suggesting that further improvements could be achieved with expanded bounds. Importantly, this study only adjusted the negative side of the VRFB. We hypothesize that the procedure herein could also be applied in tandem with the positive side electrode to potentially yield greater increases in system power density and efficiency.

This model and simulation procedure only considers a single flow rate, active species concentration, and flow field for one electrode type. Thus, there are opportunities to quantify the correlations between additional cell-level parameters and cell performance, which can, in turn, be leveraged in electrode development to improve overall cell power efficiency. Using the statistic correlation herein, this approach can be further applied to additional design components of the RFB. In particular, RFB scale-up that includes multiple stacks and shunt currents can also be investigated to potential additional trends not previously registered in literature. This can, in part, aid in the development of industrial-scale RFBs for grid applications.

Finally, while these simulations are grounded in first-principle equations, they do not supplant experimentation. Statistical calculations on large data sets originating from simulations or experimentation can reveal physical trends previously obfuscated by competing coupled physics. In particular, these simulation-based results convey parameter importance with respect to the governing power density and fluid dynamic performance, which can be beneficial in future macrohomogeneous electrode development.

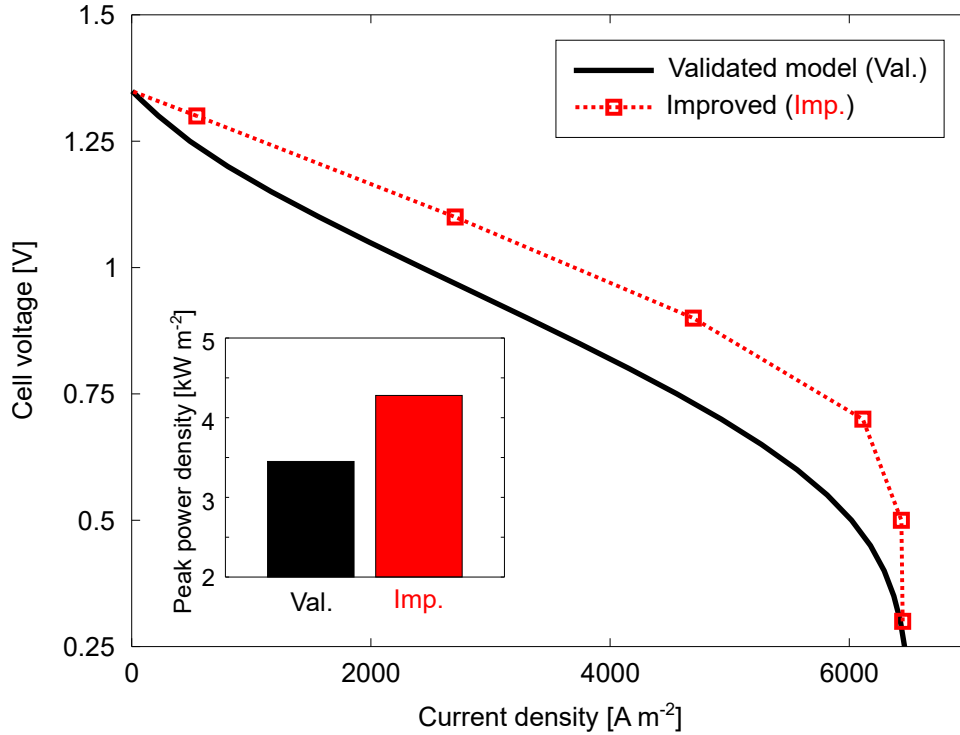


Figure 11: The polarization curve of the experimental results compared to the improved negative electrode configuration. The inset bar graph depicts the peak power density values. “Val.” and “Imp.” refer to the validated model and improved configurations, respectively.

6. Conclusions

Tuning the electrode structure can provide an avenue to cost-effective RFB systems with high discharge power density and low pressure drop. To enable high-throughput screening of a broad design space, multiphysics simulations are a facile medium with which to quickly test a range of electrode configurations that may not be commercially available. Herein, we presented a parametric analysis on the major, macrohomogeneous electrode properties of the negative electrode in a VRFB. For computational feasibility, a full 3D model was simplified with a reduced 2D model on the yz plane based on the assumption of neglecting the variation of physical quantities along the x direction. The developed reduced planar model was numerically verified and experimentally validated through in-depth comparison of polarization curves and major physical responses. In summary, our 2D

model captures the fluid dynamic and electrochemical behavior of the full 3D model.

The negative electrode parameters, i.e., $H_{e,-}$, ε_- , $d_{f,-}$, $A_{V,-}$, and k_- , were altered to generate 7350 polarization curves across six cell voltages using the 2D model. This generated a data set of 44 100 different electrode-voltage-current relationships that were quantitatively correlated using the Kendall τ rank coefficient. The $A_{V,-}$ was shown to have the largest positive correlation with the current density among all electrode parameters investigated here. Conversely, the $H_{e,-}$ had the largest negative correlation with the pressure drop across the electrode, but reveals a strong positive correlation with the current density. In assessing the flow cell net power efficiency, the improved macrohomogeneous electrode had electrochemistry-favored $A_{V,-}$, k_- , and ε_- values and fluid dynamics-favored $d_{f,-}$ values, where the $H_{e,-}$ acted as a trade-off parameter. Importantly, these correlations do not necessarily imply causation but rather a metric of importance to guide future electrode designs. Instead, large validated simulation data sets can present a route for computing further simplified and high-throughput predictive models. The addition of robust statistical analyses can thus be used as a tool for determining specific property importance. Additionally, the application herein solely focused on steady-state polarization measurements; but, this statistical framework can also be applied to dynamic processes, such as battery cycling and impedance measurements, to extend the analysis to transient behavior.

The presented approach has the potential to influence the technological development of advanced electrode designs and data science, such as data-driven modeling and machine learning. The extension of this framework to electrode and flow field designs in RFBs can boost the unexplored potential of combined design optimization and physics-informed data-driven modeling. Future studies will focus on multi-scale modeling and design optimization of flow field focused on minimizing overpotential losses within the system.

7. Acknowledgments

K.M.T., Y.-M.C., and F.R.B. are thankful for the financial support from the Joint Center for Energy Storage Research, an Energy Innovation Hub funded by the U.S. Department of Energy, Office of Science, Basic Energy (De-AC02-06CH11357). K.M.T. acknowledges additional funding from the U.S. National Science Foundation Graduate Research Fellowship (1122374). A.F.-C. acknowledges funding from the Dutch Research Council (NWO) for the Veni Grant (17324). Z.C.

thanks Politecnico di Torino for its support. R.B. acknowledges the University of California, San Diego for its support.

8. CRediT authorship contribution statement

Ziqiang Cheng: Conceptualization, Methodology, Validation, Formal analysis, Investigation, Data curation, Writing - original draft, Writing - review & editing, Visualization. **Kevin M. Tenny:** Conceptualization, Methodology, Validation, Formal analysis, Investigation, Writing - original draft, Writing - review & editing, Visualization. **Alberto Pizzolato:** Methodology, Resources, Writing - review & editing. **Antoni Forner-Cuenca:** Writing - review & editing, Supervision. **Vittorio Verda:** Resources. **Yet-Ming Chiang:** Resources. **Fikile R. Brushett:** Resources, Writing - Writing - review & editing, Supervision. **Reza Behrou:** Conceptualization, Methodology, Writing - original draft, Writing - review & editing, Supervision.

References

- [1] T. R. Ayodele, A. Jimoh, J. L. Munda, A. J. Tehile, Challenges of Grid Integration of Wind Power on Power System Grid Integrity: A Review, *International Journal of Renewable Energy Research (IJRER)* 2 (2012) 618–626. URL: <https://ijrer.com/index.php/ijrer/article/view/317>, number: 4.
- [2] M. Bragard, N. Soltau, S. Thomas, R. W. De Doncker, The Balance of Renewable Sources and User Demands in Grids: Power Electronics for Modular Battery Energy Storage Systems, *IEEE Transactions on Power Electronics* 25 (2010) 3049–3056. doi:[10.1109/TPEL.2010.2085455](https://doi.org/10.1109/TPEL.2010.2085455).
- [3] M. S. Ziegler, J. M. Mueller, G. D. Pereira, J. Song, M. Ferrara, Y.-M. Chiang, J. E. Trancik, Storage Requirements and Costs of Shaping Renewable Energy Toward Grid Decarbonization, *Joule* 3 (2019) 2134–2153. doi:[10.1016/j.joule.2019.06.012](https://doi.org/10.1016/j.joule.2019.06.012).
- [4] A. Z. Weber, M. M. Mench, J. P. Meyers, P. N. Ross, J. T. Gostick, Q. Liu, Redox flow batteries: A review, *Journal of Applied Electrochemistry* 41 (2011) 1137–1164. doi:[10.1007/s10800-011-0348-2](https://doi.org/10.1007/s10800-011-0348-2).

- [5] M. Skyllas-Kazacos, M. H. Chakrabarti, S. A. Hajimolana, F. S. Mjalli, M. Saleem, Progress in Flow Battery Research and Development, *Journal of The Electrochemical Society* 158 (2011) R55. doi:[10.1149/1.3599565](https://doi.org/10.1149/1.3599565).
- [6] C. Ponce de León, A. Frías-Ferrer, J. González-García, D. Szánto, F. Walsh, Redox flow cells for energy conversion, *Journal of Power Sources* 160 (2006) 716–732. doi:[10.1016/j.jpowsour.2006.02.095](https://doi.org/10.1016/j.jpowsour.2006.02.095).
- [7] L. Arenas, C. Ponce de León, F. Walsh, Engineering aspects of the design, construction and performance of modular redox flow batteries for energy storage, *Journal of Energy Storage* 11 (2017) 119–153. doi:[10.1016/j.est.2017.02.007](https://doi.org/10.1016/j.est.2017.02.007).
- [8] Z. Yang, J. Zhang, M. C. W. Kintner-Meyer, X. Lu, D. Choi, J. P. Lemmon, J. Liu, Electrochemical Energy Storage for Green Grid, *Chemical Reviews* 111 (2011) 3577–3613. doi:[10.1021/cr100290v](https://doi.org/10.1021/cr100290v).
- [9] P. Leung, X. Li, C. Ponce de León, L. Berlouis, C. T. J. Low, F. C. Walsh, Progress in redox flow batteries, remaining challenges and their applications in energy storage, *RSC Advances* 2 (2012) 10125. doi:[10.1039/c2ra21342g](https://doi.org/10.1039/c2ra21342g).
- [10] H. Zhang, W. Lu, X. Li, Progress and Perspectives of Flow Battery Technologies, *Electrochemical Energy Reviews* 2 (2019) 492–506. doi:[10.1007/s41918-019-00047-1](https://doi.org/10.1007/s41918-019-00047-1).
- [11] B. Dunn, H. Kamath, J.-M. Tarascon, Electrical Energy Storage for the Grid: A Battery of Choices, *Science* 334 (2011) 928–935. doi:[10.1126/science.1212741](https://doi.org/10.1126/science.1212741).
- [12] X. Luo, J. Wang, M. Dooner, J. Clarke, Overview of current development in electrical energy storage technologies and the application potential in power system operation, *Applied Energy* 137 (2015) 511–536. doi:[10.1016/j.apenergy.2014.09.081](https://doi.org/10.1016/j.apenergy.2014.09.081).
- [13] X. Li, H. Zhang, Z. Mai, H. Zhang, I. Vankelecom, Ion exchange membranes for vanadium redox flow battery (VRB) applications, *Energy & Environmental Science* 4 (2011) 1147–1160. doi:[10.1039/c0ee00770f](https://doi.org/10.1039/c0ee00770f).
- [14] Q. Xu, T. Zhao, P. Leung, Numerical investigations of flow field designs for vanadium redox flow batteries, *Applied Energy* 105 (2013) 47–56. doi:[10.1016/j.apenergy.2012.12.041](https://doi.org/10.1016/j.apenergy.2012.12.041).

- [15] W. Wang, Q. Luo, B. Li, X. Wei, L. Li, Z. Yang, Recent Progress in Redox Flow Battery Research and Development, *Advanced Functional Materials* 23 (2013) 970–986. doi:[10.1002/adfm.201200694](https://doi.org/10.1002/adfm.201200694).
- [16] C. Ding, H. Zhang, X. Li, T. Liu, F. Xing, Vanadium Flow Battery for Energy Storage: Prospects and Challenges, *The Journal of Physical Chemistry Letters* 4 (2013) 1281–1294. doi:[10.1021/jz4001032](https://doi.org/10.1021/jz4001032).
- [17] K. J. Kim, M.-S. Park, Y.-J. Kim, J. H. Kim, S. X. Dou, M. Skyllas-Kazacos, A technology review of electrodes and reaction mechanisms in vanadium redox flow batteries, *Journal of Materials Chemistry A* 3 (2015) 16913–16933. doi:[10.1039/C5TA02613J](https://doi.org/10.1039/C5TA02613J).
- [18] M. Ulaganathan, V. Aravindan, Q. Yan, S. Madhavi, M. Skyllas-Kazacos, T. M. Lim, Recent Advancements in All-Vanadium Redox Flow Batteries, *Advanced Materials Interfaces* 3 (2016) 1500309. doi:[10.1002/admi.201500309](https://doi.org/10.1002/admi.201500309).
- [19] K. Lourenssen, J. Williams, F. Ahmadpour, R. Clemmer, S. Tasnim, Vanadium redox flow batteries: A comprehensive review, *Journal of Energy Storage* 25 (2019) 100844. doi:[10.1016/j.est.2019.100844](https://doi.org/10.1016/j.est.2019.100844).
- [20] L. F. Castañeda, F. C. Walsh, J. L. Nava, C. Ponce de León, Graphite felt as a versatile electrode material: Properties, reaction environment, performance and applications, *Electrochimica Acta* 258 (2017) 1115–1139. URL: <http://www.sciencedirect.com/science/article/pii/S0013468617325276>. doi:[10.1016/j.electacta.2017.11.165](https://doi.org/10.1016/j.electacta.2017.11.165).
- [21] K. V. Greco, A. Forner-Cuenca, A. Mularczyk, J. Eller, F. R. Brushett, Elucidating the Nuanced Effects of Thermal Pretreatment on Carbon Paper Electrodes for Vanadium Redox Flow Batteries, *ACS Applied Materials & Interfaces* 10 (2018) 44430–44442. doi:[10.1021/acsami.8b15793](https://doi.org/10.1021/acsami.8b15793).
- [22] X. L. Zhou, Y. K. Zeng, X. B. Zhu, L. Wei, T. S. Zhao, A high-performance dual-scale porous electrode for vanadium redox flow batteries, *Journal of Power Sources* 325 (2016) 329–336. doi:[10.1016/j.jpowsour.2016.06.048](https://doi.org/10.1016/j.jpowsour.2016.06.048).
- [23] Q. H. Liu, G. M. Grim, A. B. Papandrew, A. Turhan, T. A. Zawodzinski, M. M. Mench, High Performance Vanadium Redox Flow Batteries with Optimized Electrode Configuration

- and Membrane Selection, *Journal of The Electrochemical Society* 159 (2012) A1246–A1252. doi:[10.1149/2.051208jes](https://doi.org/10.1149/2.051208jes).
- [24] M. MacDonald, R. M. Darling, Modeling flow distribution and pressure drop in redox flow batteries, *AIChE Journal* 64 (2018) 3746–3755. doi:[10.1002/aic.16330](https://doi.org/10.1002/aic.16330).
- [25] T.-C. Chang, J.-P. Zhang, Y.-K. Fuh, Electrical, mechanical and morphological properties of compressed carbon felt electrodes in vanadium redox flow battery, *Journal of Power Sources* 245 (2014) 66–75. doi:[10/ggh5h5](https://doi.org/10/ggh5h5).
- [26] R. Gundlapalli, S. Jayanti, Effect of electrode compression and operating parameters on the performance of large vanadium redox flow battery cells, *Journal of Power Sources* 427 (2019) 231–242. doi:[10.1016/j.jpowsour.2019.04.059](https://doi.org/10.1016/j.jpowsour.2019.04.059).
- [27] S.-K. Park, J. Shim, J. H. Yang, C.-S. Jin, B. S. Lee, Y.-S. Lee, K.-H. Shin, J.-D. Jeon, The influence of compressed carbon felt electrodes on the performance of a vanadium redox flow battery, *Electrochimica Acta* 116 (2014) 447–452. doi:[10.1016/j.electacta.2013.11.073](https://doi.org/10.1016/j.electacta.2013.11.073).
- [28] Q. Wang, Z. G. Qu, Z. Y. Jiang, W. W. Yang, Experimental study on the performance of a vanadium redox flow battery with non-uniformly compressed carbon felt electrode, *Applied Energy* 213 (2018) 293–305. doi:[10/gc5jtw](https://doi.org/10/gc5jtw).
- [29] P. C. Ghimire, A. Bhattarai, R. Schweiss, G. G. Scherer, N. Wai, Q. Yan, A comprehensive study of electrode compression effects in all vanadium redox flow batteries including locally resolved measurements, *Applied Energy* 230 (2018) 974–982. doi:[10/gfmphn](https://doi.org/10/gfmphn).
- [30] R. Banerjee, N. Bevilacqua, L. Eifert, R. Zeis, Characterization of carbon felt electrodes for vanadium redox flow batteries – A pore network modeling approach, *Journal of Energy Storage* 21 (2019) 163–171. doi:[10.1016/j.est.2018.11.014](https://doi.org/10.1016/j.est.2018.11.014).
- [31] Y. Zhou, L. Liu, Y. Shen, L. Wu, L. Yu, F. Liang, J. Xi, Carbon dots promoted vanadium flow batteries for all-climate energy storage, *Chemical Communications* 53 (2017) 7565–7568. doi:[10.1039/C7CC00691H](https://doi.org/10.1039/C7CC00691H).
- [32] P. Huang, W. Ling, H. Sheng, Y. Zhou, X. Wu, X.-X. Zeng, X. Wu, Y.-G. Guo, Heteroatom-doped electrodes for all-vanadium redox flow batteries with ultralong lifespan, *Journal of Materials Chemistry A* 6 (2017) 41–44. doi:[10.1039/C7TA07358E](https://doi.org/10.1039/C7TA07358E).

- [33] Y. Liu, Y. Shen, L. Yu, L. Liu, F. Liang, X. Qiu, J. Xi, Holey-engineered electrodes for advanced vanadium flow batteries, *Nano Energy* 43 (2018) 55–62. doi:[10.1016/j.nanoen.2017.11.012](https://doi.org/10.1016/j.nanoen.2017.11.012).
- [34] H. R. Jiang, W. Shyy, L. Zeng, R. H. Zhang, T. S. Zhao, Highly efficient and ultra-stable boron-doped graphite felt electrodes for vanadium redox flow batteries, *Journal of Materials Chemistry A* 6 (2018) 13244–13253. doi:[10.1039/C8TA03388A](https://doi.org/10.1039/C8TA03388A).
- [35] H. R. Jiang, Y. K. Zeng, M. C. Wu, W. Shyy, T. S. Zhao, A uniformly distributed bismuth nanoparticle-modified carbon cloth electrode for vanadium redox flow batteries, *Applied Energy* 240 (2019) 226–235. doi:[10.1016/j.apenergy.2019.02.051](https://doi.org/10.1016/j.apenergy.2019.02.051).
- [36] H. R. Jiang, J. Sun, L. Wei, M. C. Wu, W. Shyy, T. S. Zhao, A high power density and long cycle life vanadium redox flow battery, *Energy Storage Materials* 24 (2020) 529–540. doi:[10.1016/j.ensm.2019.07.005](https://doi.org/10.1016/j.ensm.2019.07.005).
- [37] L. Zeng, J. Sun, T. S. Zhao, Y. X. Ren, L. Wei, Balancing the specific surface area and mass diffusion property of electrospun carbon fibers to enhance the cell performance of vanadium redox flow battery, *International Journal of Hydrogen Energy* 45 (2020) 12565–12576. doi:[10.1016/j.ijhydene.2020.02.177](https://doi.org/10.1016/j.ijhydene.2020.02.177).
- [38] R. K. Gautam, M. Kapoor, A. Verma, Tactical Surface Modification of a 3D Graphite Felt as an Electrode of Vanadium Redox Flow Batteries with Enhanced Electrolyte Utilization and Fast Reaction Kinetics, *Energy & Fuels* 34 (2020) 5060–5071. doi:[10.1021/acs.energyfuels.0c00701](https://doi.org/10.1021/acs.energyfuels.0c00701).
- [39] R. K. Gautam, A. Verma, Uniquely designed surface nanocracks for highly efficient and ultra-stable graphite felt electrode for vanadium redox flow battery, *Materials Chemistry and Physics* (2020) 123178. doi:[10.1016/j.matchemphys.2020.123178](https://doi.org/10.1016/j.matchemphys.2020.123178).
- [40] Q. Zheng, H. Zhang, F. Xing, X. Ma, X. Li, G. Ning, A three-dimensional model for thermal analysis in a vanadium flow battery, *Applied Energy* 113 (2014) 1675–1685. doi:[10.1016/j.apenergy.2013.09.021](https://doi.org/10.1016/j.apenergy.2013.09.021).
- [41] C. Yin, S. Guo, H. Fang, J. Liu, Y. Li, H. Tang, Numerical and experimental studies of stack shunt current for vanadium redox flow battery, *Applied Energy* 151 (2015) 237–248. URL:

<https://doi.org/10.1016/j.apenergy.2015.04.080>, doi:[10.1016/j.apenergy.2015.04.080](https://doi.org/10.1016/j.apenergy.2015.04.080).

- [42] M. Messaggi, P. Canzi, R. Mereu, A. Baricci, F. Inzoli, A. Casalegno, M. Zago, Analysis of flow field design on vanadium redox flow battery performance: Development of 3D computational fluid dynamic model and experimental validation, *Applied Energy* 228 (2018) 1057–1070. doi:[10.1016/J.APENERGY.2018.06.148](https://doi.org/10.1016/J.APENERGY.2018.06.148).
- [43] M. R. Gerhardt, A. A. Wong, M. J. Aziz, The Effect of Interdigitated Channel and Land Dimensions on Flow Cell Performance, *Journal of The Electrochemical Society* 165 (2018) A2625–A2643. doi:[10.1149/2.0471811jes](https://doi.org/10.1149/2.0471811jes).
- [44] C. Yin, Y. Gao, G. Xie, T. Li, H. Tang, Three dimensional multi-physical modeling study of interdigitated flow field in porous electrode for vanadium redox flow battery, *Journal of Power Sources* 438 (2019) 227023. doi:[10.1016/j.jpowsour.2019.227023](https://doi.org/10.1016/j.jpowsour.2019.227023).
- [45] J. Lee, J. Kim, H. Park, Numerical simulation of the power-based efficiency in vanadium redox flow battery with different serpentine channel size, *International Journal of Hydrogen Energy* 44 (2019) 29483–29492. doi:[10.1016/j.ijhydene.2019.05.013](https://doi.org/10.1016/j.ijhydene.2019.05.013).
- [46] C. Yuan, F. Xing, Q. Zheng, H. Zhang, X. Li, X. Ma, Factor analysis of the uniformity of the transfer current density in vanadium flow battery by an improved three-dimensional transient model, *Energy* 194 (2020) 116839. URL: <https://doi.org/10.1016/j.energy.2019.116839>. doi:[10.1016/j.energy.2019.116839](https://doi.org/10.1016/j.energy.2019.116839).
- [47] D. Zhang, A. Forner-Cuenca, O. O. Taiwo, V. Yufit, F. R. Brushett, N. P. Brandon, S. Gu, Q. Cai, Understanding the role of the porous electrode microstructure in redox flow battery performance using an experimentally validated 3D pore-scale lattice Boltzmann model, *Journal of Power Sources* 447 (2020) 227249. doi:[10.1016/j.jpowsour.2019.227249](https://doi.org/10.1016/j.jpowsour.2019.227249).
- [48] A. Shah, M. Watt-Smith, F. Walsh, A dynamic performance model for redox-flow batteries involving soluble species, *Electrochimica Acta* 53 (2008) 8087–8100. doi:[10.1016/j.electacta.2008.05.067](https://doi.org/10.1016/j.electacta.2008.05.067).
- [49] D. You, H. Zhang, J. Chen, A simple model for the vanadium redox battery, *Electrochimica Acta* 54 (2009) 6827–6836. doi:[10.1016/j.electacta.2009.06.086](https://doi.org/10.1016/j.electacta.2009.06.086).

- [50] K. W. Knehr, E. Agar, C. R. Dennison, A. R. Kalidindi, E. C. Kumbur, A Transient Vanadium Flow Battery Model Incorporating Vanadium Crossover and Water Transport through the Membrane, *Journal of The Electrochemical Society* 159 (2012) A1446–A1459. doi:[10.1149/2.017209jes](https://doi.org/10.1149/2.017209jes).
- [51] K. Bromberger, J. Kaunert, T. Smolinka, A Model for All-Vanadium Redox Flow Batteries: Introducing Electrode-Compression Effects on Voltage Losses and Hydraulics, *Energy Technology* 2 (2014) 64–76. doi:[10.1002/ente.201300114](https://doi.org/10.1002/ente.201300114).
- [52] Q. Xu, T. Zhao, C. Zhang, Effects of SOC-dependent electrolyte viscosity on performance of vanadium redox flow batteries, *Applied Energy* 130 (2014) 139–147. doi:[10.1016/j.apenergy.2014.05.034](https://doi.org/10.1016/j.apenergy.2014.05.034).
- [53] A. Sharma, C. Ling, E. Birgersson, M. Vynnycky, M. Han, Verified reduction of dimensionality for an all-vanadium redox flow battery model, *Journal of Power Sources* 279 (2015) 345–350. doi:[10.1016/j.jpowsour.2015.01.019](https://doi.org/10.1016/j.jpowsour.2015.01.019).
- [54] A. Khazaeli, A. Vatani, N. Tahouni, M. H. Panjeshahi, Numerical investigation and thermodynamic analysis of the effect of electrolyte flow rate on performance of all vanadium redox flow batteries, *Journal of Power Sources* 293 (2015) 599–612. doi:[10.1016/j.jpowsour.2015.05.100](https://doi.org/10.1016/j.jpowsour.2015.05.100).
- [55] Y. A. Gandomi, D. S. Aaron, T. A. Zawodzinski, M. M. Mench, In Situ Potential Distribution Measurement and Validated Model for All-Vanadium Redox Flow Battery, *Journal of The Electrochemical Society* 163 (2016) A5188–A5201. doi:[10.1149/2.0211601jes](https://doi.org/10.1149/2.0211601jes).
- [56] X. Zhou, T. Zhao, L. An, Y. Zeng, L. Wei, Modeling of ion transport through a porous separator in vanadium redox flow batteries, *Journal of Power Sources* 327 (2016) 67–76. doi:[10.1016/j.jpowsour.2016.07.046](https://doi.org/10.1016/j.jpowsour.2016.07.046).
- [57] B. Zhang, Y. Lei, B. Bai, A. Xu, T. Zhao, A two-dimensional mathematical model for vanadium redox flow battery stacks incorporating nonuniform electrolyte distribution in the flow frame, *Applied Thermal Engineering* 151 (2019) 495–505. doi:[10.1016/j.applthermaleng.2019.02.037](https://doi.org/10.1016/j.applthermaleng.2019.02.037).

- [58] B. Zhang, Y. Lei, B. Bai, T. Zhao, A two-dimensional model for the design of flow fields in vanadium redox flow batteries, *International Journal of Heat and Mass Transfer* 135 (2019) 460–469. doi:[10.1016/j.ijheatmasstransfer.2019.02.008](https://doi.org/10.1016/j.ijheatmasstransfer.2019.02.008).
- [59] M. D. R. Kok, A. Khalifa, J. T. Gostick, Multiphysics Simulation of the Flow Battery Cathode: Cell Architecture and Electrode Optimization, *Journal of The Electrochemical Society* 163 (2016) A1408–A1419. doi:[10.1149/2.1281607jes](https://doi.org/10.1149/2.1281607jes).
- [60] S. Tsushima, T. Suzuki, Modeling and Simulation of Vanadium Redox Flow Battery with Interdigitated Flow Field for Optimizing Electrode Architecture, *Journal of The Electrochemical Society* 167 (2020) 020553. doi:[10.1149/1945-7111/ab6dd0](https://doi.org/10.1149/1945-7111/ab6dd0).
- [61] J. Newman, K. E. Thomas-Alyea, *Electrochemical Systems*, John Wiley & Sons, 2004.
- [62] H. K. Versteeg, W. Malalasekera, *An Introduction to Computational Fluid Dynamics: The Finite Volume Method*, 2nd ed ed., Pearson Education Ltd, Harlow, England ; New York, 2007.
- [63] M. K. Das, P. P. Mukherjee, K. Muralidhar, *Modeling Transport Phenomena in Porous Media with Applications*, Springer International Publishing, Cham, 2018.
- [64] M. Ehrhardt, An Introduction to Fluid-Porous Interface Coupling, in: K. Vafai (Ed.), *Progress in Computational Physics (PiCP) Vol: 2 Coupled Fluid Flow in Energy, Biology and Environmental Research*, BENTHAM SCIENCE PUBLISHERS, 2012, pp. 3–12. doi:[10.2174/978160805254711201010003](https://doi.org/10.2174/978160805254711201010003).
- [65] M. M. Tomadakis, T. J. Robertson, Viscous Permeability of Random Fiber Structures: Comparison of Electrical and Diffusional Estimates with Experimental and Analytical Results, *Journal of Composite Materials* 39 (2005) 163–188. doi:[10.1177/0021998305046438](https://doi.org/10.1177/0021998305046438).
- [66] R. P. O’Hayre, S.-W. Cha, W. G. Colella, F. B. Prinz, *Fuel Cell Fundamentals*, third edition ed., Wiley, Hoboken, New Jersey, 2016.
- [67] F. C. Walsh, The Kinetics of Electrode Reactions: Part I—General Considerations and Electron Transfer Control, *Transactions of the IMF* 70 (1992) 50–54. doi:[10.1080/00202967.1992.11870941](https://doi.org/10.1080/00202967.1992.11870941).

- [68] F. C. Walsh, The Kinetics of Electrode Reactions: Part II—Mass Transfer and Mixed Control, *Transactions of the IMF* 70 (1992) 95–99. doi:[10.1080/00202967.1992.11870952](https://doi.org/10.1080/00202967.1992.11870952).
- [69] E. Agar, K. W. Knehr, D. Chen, M. A. Hickner, E. C. Kumbur, Species transport mechanisms governing capacity loss in vanadium flow batteries: Comparing Nafion® and sulfonated Radel membranes, *Electrochimica Acta* 98 (2013) 66–74. doi:[10.1016/j.electacta.2013.03.030](https://doi.org/10.1016/j.electacta.2013.03.030).
- [70] K. Knehr, E. Kumbur, Open circuit voltage of vanadium redox flow batteries: Discrepancy between models and experiments, *Electrochemistry Communications* 13 (2011) 342–345. doi:[10.1016/j.elecom.2011.01.020](https://doi.org/10.1016/j.elecom.2011.01.020).
- [71] M. Skyllas-Kazacos, L. Cao, M. Kazacos, N. Kausar, A. Mousa, Vanadium Electrolyte Studies for the Vanadium Redox Battery-A Review, *ChemSusChem* 9 (2016) 1521–1543. doi:[10.1002/cssc.201600102](https://doi.org/10.1002/cssc.201600102).
- [72] D. A. Knopf, B. P. Luo, U. K. Krieger, T. Koop, Thermodynamic Dissociation Constant of the Bisulfate Ion from Raman and Ion Interaction Modeling Studies of Aqueous Sulfuric Acid at Low Temperatures, *The Journal of Physical Chemistry A* 107 (2003) 4322–4332. doi:[10.1021/jp027775+](https://doi.org/10.1021/jp027775+).
- [73] D. Schmal, J. Van Erkel, P. J. Van Duin, Mass transfer at carbon fibre electrodes, *Journal of Applied Electrochemistry* 16 (1986) 422–430. doi:[10.1007/bf01008853](https://doi.org/10.1007/bf01008853).
- [74] C. H. Hamann, A. Hamnett, W. Vielstich, *Electrochemistry*, 2nd ed., Wiley-VCH Verlag GmbH, Weinheim, Germany, 2007.
- [75] M. W. Verbrugge, R. F. Hill, Ion and Solvent Transport in Ion-Exchange Membranes: I. A Macrohomogeneous Mathematical Model, *J. Electrochem. Soc.* 137 (1990) 8. doi:[10.1149/1.2086573](https://doi.org/10.1149/1.2086573).
- [76] M. W. Verbrugge, R. F. Hill, Experimental and theoretical investigation of perfluorosulfonic acid membranes equilibrated with aqueous sulfuric acid solutions, *The Journal of Physical Chemistry* 92 (1988) 6778–6783. doi:[10.1021/j100334a056](https://doi.org/10.1021/j100334a056).
- [77] X. Ke, J. M. Prahl, J. I. D. Alexander, J. S. Wainright, T. A. Zawodzinski, R. F. Savinell, Rechargeable redox flow batteries: Flow fields, stacks and design considerations, *Chemical Society Reviews* 47 (2018) 8721–8743. doi:[10.1039/C8CS00072G](https://doi.org/10.1039/C8CS00072G).

- [78] R. M. Darling, P. Badrinarayanan, Oxygen Transport in Polymer-Electrolyte Fuel Cells with Interdigitated Air Channels in Porous Bipolar Plates, *Journal of The Electrochemical Society* 158 (2011) B54. doi:[10.1149/1.3509159](https://doi.org/10.1149/1.3509159).
- [79] A. Akers, M. Gassman, R. Smith, *Hydraulic Power System Analysis*, zeroth ed., CRC Press, 2006. doi:[10.1201/9781420014587](https://doi.org/10.1201/9781420014587).
- [80] Y. Zhang, J. Zhao, P. Wang, M. Skyllas-Kazacos, B. Xiong, R. Badrinarayanan, A comprehensive equivalent circuit model of all-vanadium redox flow battery for power system analysis, *Journal of Power Sources* 290 (2015) 14–24. doi:[10.1016/j.jpowsour.2015.04.169](https://doi.org/10.1016/j.jpowsour.2015.04.169).
- [81] K. B. Shyam Prasad, P. V. Suresh, S. Jayanti, A hydrodynamic network model for interdigitated flow fields, *International Journal of Hydrogen Energy* 34 (2009) 8289–8301. doi:[10.1016/j.ijhydene.2009.07.107](https://doi.org/10.1016/j.ijhydene.2009.07.107).
- [82] G. Brown, The History of the Darcy-Weisbach Equation for Pipe Flow Resistance, *Environmental and Water Resources History* (2003) 34–43. doi:[10.1061/40650\(2003\)4](https://doi.org/10.1061/40650(2003)4).
- [83] F. White, *Fluid Mechanics*, McGraw-Hill Series in Mechanical Engineering, 7 ed., McGraw Hill, 2011.
- [84] C. K. Alexander, M. N. O. Sadiku, *Fundamentals of Electric Circuits*, 5th ed ed., McGraw-Hill, New York, NY, 2013.
- [85] R. M. Darling, M. L. Perry, The Influence of Electrode and Channel Configurations on Flow Battery Performance, *Journal of The Electrochemical Society* 161 (2014) A1381–A1387. doi:[10.1149/2.0941409jes](https://doi.org/10.1149/2.0941409jes).
- [86] J. D. Milshtein, K. M. Tenny, J. L. Barton, J. Drake, R. M. Darling, F. R. Brushett, Quantifying Mass Transfer Rates in Redox Flow Batteries, *Journal of The Electrochemical Society* 164 (2017) E3265–E3275. doi:[10.1149/2.0201711jes](https://doi.org/10.1149/2.0201711jes).
- [87] R. M. Darling, Pseudo-Steady-State Flow Battery Experiments, ECS Meeting (2013).
- [88] COMSOL Multiphysics v. 5.3a, COMSOL AB, Stockholm, Sweden, 2017.

- [89] L. P. Franca, S. L. Frey, T. J. R. Hughes, Stabilized finite element methods: I. Application to the advective-diffusive model, *Computer Methods in Applied Mechanics and Engineering* 95 (1992) 253–276. doi:[10.1016/0045-7825\(92\)90143-8](https://doi.org/10.1016/0045-7825(92)90143-8).
- [90] L. P. Franca, S. L. Frey, Stabilized finite element methods: II. The incompressible Navier-Stokes equations, *Computer Methods in Applied Mechanics and Engineering* 99 (1992) 209–233. doi:[10.1016/0045-7825\(92\)90041-H](https://doi.org/10.1016/0045-7825(92)90041-H).
- [91] C. Johnson, J. Saranen, Streamline Diffusion Methods for the Incompressible Euler and Navier-Stokes Equations, *Mathematics of Computation* 47 (1986) 1–18. doi:[10.2307/2008079](https://doi.org/10.2307/2008079).
- [92] A. C. Galeão, E. G. Dutra do Carmo, A consistent approximate upwind Petrov-Galerkin method for convection-dominated problems, *Computer Methods in Applied Mechanics and Engineering* 68 (1988) 83–95. doi:[10.1016/0045-7825\(88\)90108-9](https://doi.org/10.1016/0045-7825(88)90108-9).
- [93] R. Peyret, *Handbook of Computational Fluid Mechanics*, Elsevier, 1996. doi:[10.1016/B978-0-12-553010-1.X5000-2](https://doi.org/10.1016/B978-0-12-553010-1.X5000-2).
- [94] W. L. Briggs, V. E. Henson, S. F. McCormick, *A Multigrid Tutorial: Second Edition*, 2 ed., Society for Industrial and Applied Mathematics (SIAM, 3600 Market Street, Floor 6, Philadelphia, PA 19104), 2000.
- [95] A. Forner-Cuenca, E. E. Penn, A. M. Oliveira, F. R. Brushett, Exploring the Role of Electrode Microstructure on the Performance of Non-Aqueous Redox Flow Batteries, *Journal of The Electrochemical Society* 166 (2019) A2230–A2241. doi:[10.1149/2.0611910jes](https://doi.org/10.1149/2.0611910jes).
- [96] S. Yadav, *Fabrication and Characterization of Novel Flow Battery Electrodes Using Electrospinning*, Thesis, University of Waterloo, 2018.
- [97] X. Li, J. Xiong, A. Tang, Y. Qin, J. Liu, C. Yan, Investigation of the use of electrolyte viscosity for online state-of-charge monitoring design in vanadium redox flow battery, *Applied Energy* 211 (2018) 1050–1059. doi:[10.1016/j.apenergy.2017.12.009](https://doi.org/10.1016/j.apenergy.2017.12.009).
- [98] S. Yin, L. Zhou, X. Du, Y. Yang, Influence of temperature on performance of all vanadium redox flow battery: Analysis of ionic mass transfer, *Ionics* 25 (2019) 593–606. doi:[10.1007/s11581-018-2626-z](https://doi.org/10.1007/s11581-018-2626-z).

- [99] T. Yamamura, N. Watanabe, T. Yano, Y. Shiokawa, Electron-transfer kinetics of $\text{Np}^{3+}/\text{Np}^{4+}$, $\text{NpO}_2^{2+}/\text{NpO}_2^{2+}$, $\text{V}^{2+}/\text{V}^{3+}$, and $\text{VO}_2^{+}/\text{VO}_2^{+}$ at carbon electrodes, *Journal of The Electrochemical Society* 152 (2005) A830–A836. doi:[10.1149/1.1870794](https://doi.org/10.1149/1.1870794).
- [100] H. Ishitobi, J. Saito, S. Sugawara, K. Oba, N. Nakagawa, Visualized cell characteristics by a two-dimensional model of vanadium redox flow battery with interdigitated channel and thin active electrode, *Electrochimica Acta* 313 (2019) 513–522. doi:[10.1016/j.electacta.2019.04.055](https://doi.org/10.1016/j.electacta.2019.04.055).
- [101] G. Qiu, C. Dennison, K. Knehr, E. Kumbur, Y. Sun, Pore-scale analysis of effects of electrode morphology and electrolyte flow conditions on performance of vanadium redox flow batteries, *Journal of Power Sources* 219 (2012) 223–234. doi:[10.1016/j.jpowsour.2012.07.042](https://doi.org/10.1016/j.jpowsour.2012.07.042).
- [102] C. Yin, Y. Gao, S. Guo, H. Tang, A coupled three dimensional model of vanadium redox flow battery for flow field designs, *Energy* 74 (2014) 886–895. doi:[10.1016/j.energy.2014.07.066](https://doi.org/10.1016/j.energy.2014.07.066).
- [103] K. Oh, H. Yoo, J. Ko, S. Won, H. Ju, Three-dimensional, transient, nonisothermal model of all-vanadium redox flow batteries, *Energy* 81 (2015) 3–14. doi:[10.1016/J.ENERGY.2014.05.020](https://doi.org/10.1016/J.ENERGY.2014.05.020).
- [104] Q. Wang, Z. Qu, Z. Jiang, W. Yang, Numerical study on vanadium redox flow battery performance with non-uniformly compressed electrode and serpentine flow field, *Applied Energy* 220 (2018) 106–116. doi:[10.1016/j.apenergy.2018.03.058](https://doi.org/10.1016/j.apenergy.2018.03.058).
- [105] S. K. Murthy, A. K. Sharma, C. Choo, E. Birgersson, Analysis of Concentration Overpotential in an All-Vanadium Redox Flow Battery, *Journal of The Electrochemical Society* 165 (2018) A1746–A1752. doi:[10.1149/2.0681809jes](https://doi.org/10.1149/2.0681809jes).
- [106] E. Ali, H. Kwon, J. Choi, J. Lee, J. Kim, H. Park, A numerical study of electrode thickness and porosity effects in all vanadium redox flow batteries, *Journal of Energy Storage* 28 (2020) 101208. doi:[10/ggh3dn](https://doi.org/10/ggh3dn).
- [107] D. Aaron, C.-N. Sun, M. Bright, A. B. Papandrew, M. M. Mench, T. A. Zawodzinski, In Situ Kinetics Studies in All-Vanadium Redox Flow Batteries, *ECS Electrochemistry Letters* 2 (2013) A29–A31. doi:[10.1149/2.001303eel](https://doi.org/10.1149/2.001303eel).

- [108] M. A. Aziz, S. Shanmugam, Ultra-high proton/vanadium selectivity of a modified sulfonated poly(arylene ether ketone) composite membrane for all vanadium redox flow batteries, *Journal of Materials Chemistry A* 5 (2017) 16663–16671. doi:[10.1039/c7ta05155g](https://doi.org/10.1039/c7ta05155g).
- [109] D. Aaron, Z. Tang, A. B. Papandrew, T. A. Zawodzinski, Polarization curve analysis of all-vanadium redox flow batteries, *Journal of Applied Electrochemistry* 41 (2011) 1175–1182. doi:[10.1007/s10800-011-0335-7](https://doi.org/10.1007/s10800-011-0335-7).
- [110] S. M. Slade, J. R. Smith, S. A. Campbell, T. R. Ralph, C. Ponce de León, F. C. Walsh, Characterisation of a re-cast composite Nafion® 1100 series of proton exchange membranes incorporating inert inorganic oxide particles, *Electrochimica Acta* 55 (2010) 6818–6829. doi:[10.1016/j.electacta.2010.05.085](https://doi.org/10.1016/j.electacta.2010.05.085).
- [111] S. M. Slade, T. R. Ralph, C. P. de León, S. A. Campbell, F. C. Walsh, The Ionic Conductivity of a Nafion® 1100 Series of Proton-exchange Membranes Re-cast from Butan-1-ol and Propan-2-ol, *Fuel Cells* 10 (2010) 567–574. doi:[10.1002/fuce.200900118](https://doi.org/10.1002/fuce.200900118).
- [112] D. Pletcher, F. C. Walsh, Three-dimensional electrodes, *The Electrosynthesis Company Inc.:* New York (1992) 52.
- [113] R. Alkire, B. Gracon, Flow-Through Porous Electrodes, *Journal of The Electrochemical Society* 122 (1975) 1594–1601. doi:[10/cqvw4m](https://doi.org/10/cqvw4m).
- [114] F. T. Wandschneider, D. Finke, S. Grosjean, P. Fischer, K. Pinkwart, J. Tübke, H. Nirschl, Model of a vanadium redox flow battery with an anion exchange membrane and a Larminie-correction, *Journal of Power Sources* 272 (2014) 436–447. doi:[10.1016/j.jpowsour.2014.08.082](https://doi.org/10.1016/j.jpowsour.2014.08.082).
- [115] Y. Kim, Y. Y. Choi, N. Yun, M. Yang, Y. Jeon, K. J. Kim, J.-I. Choi, Activity gradient carbon felt electrodes for vanadium redox flow batteries, *Journal of Power Sources* 408 (2018) 128–135. doi:[10.1016/j.jpowsour.2018.09.066](https://doi.org/10.1016/j.jpowsour.2018.09.066).
- [116] S. König, M. Suriyah, T. Leibfried, Validating and improving a zero-dimensional stack voltage model of the Vanadium Redox Flow Battery, *Journal of Power Sources* 378 (2018) 10–18. doi:[10.1016/j.jpowsour.2017.12.014](https://doi.org/10.1016/j.jpowsour.2017.12.014).

- [117] X. Ma, H. Zhang, F. Xing, A three-dimensional model for negative half cell of the vanadium redox flow battery, *Electrochimica Acta* 58 (2011) 238–246. doi:[10.1016/j.electacta.2011.09.042](https://doi.org/10.1016/j.electacta.2011.09.042).
- [118] Y. Wang, S. C. Cho, Analysis and Three-Dimensional Modeling of Vanadium Flow Batteries, *Journal of The Electrochemical Society* 161 (2014) A1200–A1212. doi:[10.1149/2.0061409jes](https://doi.org/10.1149/2.0061409jes).
- [119] A. Tang, J. Bao, M. Skyllas-Kazacos, Studies on pressure losses and flow rate optimization in vanadium redox flow battery, *Journal of Power Sources* 248 (2014) 154–162. doi:[10.1016/j.jpowsour.2013.09.071](https://doi.org/10.1016/j.jpowsour.2013.09.071).
- [120] B. Delanghe, S. Tellier, M. Astruc, Mass transfer to a carbon or graphite felt electrode, *Electrochimica Acta* 35 (1990) 1369–1376. doi:[10.1016/0013-4686\(90\)85008-B](https://doi.org/10.1016/0013-4686(90)85008-B).
- [121] R. J. Hyndman, A. B. Koehler, Another look at measures of forecast accuracy, *International Journal of Forecasting* 22 (2006) 679–688. URL: <https://doi.org/10.1016/j.ijforecast.2006.03.001>. doi:[10.1016/j.ijforecast.2006.03.001](https://doi.org/10.1016/j.ijforecast.2006.03.001).
- [122] S. Ressel, F. Bill, L. Holtz, N. Janshen, A. Chica, T. Flower, C. Weidlich, T. Struckmann, State of charge monitoring of vanadium redox flow batteries using half cell potentials and electrolyte density, *Journal of Power Sources* 378 (2018) 776–783. doi:[10.1016/j.jpowsour.2018.01.006](https://doi.org/10.1016/j.jpowsour.2018.01.006).
- [123] Z. Wei, J. Zhao, M. Skyllas-Kazacos, B. Xiong, Dynamic thermal-hydraulic modeling and stack flow pattern analysis for all-vanadium redox flow battery, *Journal of Power Sources* 260 (2014) 89–99. doi:[10.1016/j.jpowsour.2014.02.108](https://doi.org/10.1016/j.jpowsour.2014.02.108).
- [124] B. Kleinsteinberg, S. Klick, D. U. Sauer, Empirical approach to determine open-circuit voltage of a vanadium-redox-flow battery for models, based on published data for anion-exchange and cation-exchange membranes and temperature dependency, *Journal of Energy Storage* 28 (2020) 101109. doi:[10.1016/j.est.2019.101109](https://doi.org/10.1016/j.est.2019.101109).
- [125] A. Shah, H. Al-Fetlawi, F. Walsh, Dynamic modelling of hydrogen evolution effects in the all-vanadium redox flow battery, *Electrochimica Acta* 55 (2010) 1125–1139. doi:[10.1016/j.electacta.2009.10.022](https://doi.org/10.1016/j.electacta.2009.10.022).

- [126] A. A. Shah, R. Tangirala, R. Singh, R. G. A. Wills, F. C. Walsh, A Dynamic Unit Cell Model for the All-Vanadium Flow Battery, *Journal of The Electrochemical Society* 158 (2011) A671. doi:[10.1149/1.3561426](https://doi.org/10.1149/1.3561426).
- [127] W. Chen, J. Kang, Q. Shu, Y. Zhang, Analysis of storage capacity and energy conversion on the performance of gradient and double-layered porous electrode in all-vanadium redox flow batteries, *Energy* 180 (2019) 341–355. doi:[10.1016/j.energy.2019.05.037](https://doi.org/10.1016/j.energy.2019.05.037).
- [128] A. Bourke, M. A. Miller, R. P. Lynch, X. Gao, J. Landon, J. S. Wainright, R. F. Savinell, D. N. Buckley, Electrode Kinetics of Vanadium Flow Batteries: Contrasting Responses of V^{II} - V^{III} and V^{IV} - V^{V} to Electrochemical Pretreatment of Carbon, *Journal of The Electrochemical Society* 163 (2016) A5097–A5105. doi:[10.1149/2.0131601jes](https://doi.org/10.1149/2.0131601jes).
- [129] W. H. Wang, X. D. Wang, Investigation of Ir-modified carbon felt as the positive electrode of an all-vanadium redox flow battery, *Electrochimica Acta* 52 (2007) 6755–6762. doi:[10.1016/j.electacta.2007.04.121](https://doi.org/10.1016/j.electacta.2007.04.121).
- [130] D. S. Aaron, Q. Liu, Z. Tang, G. M. Grim, A. B. Papandrew, A. Turhan, T. A. Zawodzinski, M. M. Mench, Dramatic performance gains in vanadium redox flow batteries through modified cell architecture, *Journal of Power Sources* 206 (2012) 450–453. doi:[10.1016/j.jpowsour.2011.12.026](https://doi.org/10.1016/j.jpowsour.2011.12.026).
- [131] J. T. Gostick, M. W. Fowler, M. D. Pritzker, M. A. Ioannidis, L. M. Behra, In-plane and through-plane gas permeability of carbon fiber electrode backing layers, *Journal of Power Sources* 162 (2006) 228–238. doi:[10.1016/j.jpowsour.2006.06.096](https://doi.org/10.1016/j.jpowsour.2006.06.096).
- [132] K. M. Tenny, A. Forner-Cuenca, Y.-M. Chiang, F. R. Brushett, Comparing Physical and Electrochemical Properties of Different Weave Patterns for Carbon Cloth Electrodes in Redox Flow Batteries, *Journal of Electrochemical Energy Conversion and Storage* 17 (2020). doi:[10.1115/1.4046661](https://doi.org/10.1115/1.4046661).
- [133] S. Trasatti, O. A. Petrii, Real surface area measurements in electrochemistry, *Journal of Electroanalytical Chemistry* 327 (1992) 353–376. doi:[10.1016/0022-0728\(92\)80162-W](https://doi.org/10.1016/0022-0728(92)80162-W).
- [134] S. Patankar, *Numerical Heat Transfer and Fluid Flow*, CRC Press, 2018. doi:[10.1201/9781482234213](https://doi.org/10.1201/9781482234213).

- [135] S. Bhattacharjee, W. Grosshandler, The formation of a wall jet near a high temperature wall under microgravity environment, in: ASME 1988 National Heat Transfer Conference, Volume 1, volume 1, 1988, pp. 711–716.
- [136] M. Awad, J. Lage, Extending the Bejan number to a general form, *Thermal Science* 2 (2013) 631–633. doi:[10.2298/TSCI130211032A](https://doi.org/10.2298/TSCI130211032A).
- [137] M. G. Kendall, A New Measure of Rank Correlation, *Biometrika* 30 (1938) 81–93. doi:[10.2307/2332226](https://doi.org/10.2307/2332226).
- [138] H. Yu, F. Khan, V. Garaniya, A sparse PCA for nonlinear fault diagnosis and robust feature discovery of industrial processes, *AIChE Journal* 62 (2016) 1494–1513. doi:[10.1002/aic.15136](https://doi.org/10.1002/aic.15136).
- [139] C. Croux, C. Dehon, Influence functions of the Spearman and Kendall correlation measures, *Statistical Methods & Applications* 19 (2010) 497–515. doi:[10.1007/s10260-010-0142-z](https://doi.org/10.1007/s10260-010-0142-z).

Supporting Information

Data-Driven Electrode Parameter Identification for Vanadium Redox Flow Batteries Through Experimental and Numerical Methods

Ziqiang Cheng^{a,1}, Kevin M. Tenny^{b,1}, Alberto Pizzolato^a, Antoni Forner-Cuenca^c, Vittorio Verda^a, Yet-Ming Chiang^d, Fikile R. Brushett^{b, *}, Reza Behrouf^e

^aDepartment of Energy, Politecnico di Torino, Turin, Italy

^bDepartment of Chemical Engineering, Massachusetts Institute of Technology, Cambridge, MA, USA

^cDepartment of Chemical Engineering and Chemistry, Eindhoven University of Technology, Eindhoven, Netherlands

^dDepartment of Materials Science and Engineering, Massachusetts Institute of Technology, Cambridge, MA, USA

^eDepartment of Mechanical and Aerospace Engineering, University of California San Diego, La Jolla, CA, USA

Contents

S1 Derivation of $p_{out} = p_n$	2
S1.1 Estimation of $p^? = p_n$	2
S1.2 Estimation of $p_{out} = p^?$	3
S2 Geometric Discretization of the Models	5
S2.1 Mesh Details	5
S2.2 Mesh Refinement Study	5
S3 Fitting Results	8
S4 Comparisons of 2D and 3D Simulations	9
S5 Scale-up Study on the p_{out} Estimation	14
S6 Velocity Distributions in Electrode	14
S7 Kendall Rank Correlation Coefficient	16

Corresponding authors:

Email addresses: brushett@mit.edu (Fikile R. Brushett), rbehrouf@eng.ucsd.edu (Reza Behrouf)

¹Equal contribution.

S1. Derivation of $p_{out} = p_{in}$

The detailed derivation of the relationship between p_{out} and p_{in} (i.e., Eq. (63) in the main text) is presented in this section, where p_{out} is the average pressure of an outlet channel along the channel-length direction and p_{in} denotes the inlet pressure. Unless otherwise stated, all the pressures involved in this section (e.g., $p_{()}$) are 3D pressures. The derivation is based on an equivalent circuit model, as shown in Fig. S1. As stated in Section 2.3 in the main text, the process is completed in two steps, i.e., estimation of i) $p^? = p_{in}$ and ii) $p_{out} = p^?$, where $p^?$ is the pressure at the entrance of outlet channel.

Figure S1: The equivalent circuit model approximating an arbitrary unit channel pair composed of an inlet channel, an outlet channel, and the electrode between the two, same as Fig. 4c in main text.

S1.1. Estimation of $p^? = p_{in}$

As depicted in Fig. S1, $p^?$ is located in the circuit between the two resistances associated to the first electrode and first outlet channel segments. Its value with respect to the inlet pressure (i.e., $p^? = p_{in}$) can be expressed as a function of the two resistances through basic circuit rules (i.e., Kirchoff's circuit laws [1]). Using SCAMa tool for symbolically solving circuit equations in MATLAB [2], we obtained that when $n = 2$,

$$\frac{p^?}{p_{in}}_{n=2} = \frac{R_{ch}}{2R_{ele} + R_{ch}}: \quad (S1)$$

Furthermore, when $n = 3$,

$$\frac{p^?}{p_{in}}_{n=3} = \frac{\frac{R_{ch}^3}{2} + 6 R_{ch}^2 R_{ele} + \frac{27 R_{ch} R_{ele}^2}{2}}{\frac{R_{ch}^3}{2} + \frac{15 R_{ch}^2 R_{ele}}{2} + 27 R_{ch} R_{ele}^2 + 27 R_{ele}^3}: \quad (S2)$$

It can be seen that the expression becomes more complex as n increases. Those for $n = 4$ are not displayed here due to their over-complexities. However, it can be seen that they show obvious

converging trend when n further increases. As shown in Fig. S2, where the numerical value of the ratio is calculated and compared for different n , the relative difference between two successive points is below 1% when n reaches 6. Hence, we can reasonably consider $p^2 = p_{in}$ as the final convergent value, acting as a reference to measure the accuracy of the previous simpler expressions. To this end, Eq. (S1) for $n = 2$ is preferred as it has the simplest form and acceptable error (less than 5%).

Figure S2: Variation of the calculated $p^2 = p_{in}$ with respect to different n from 2 to 6. All the necessary parameters for the calculation are listed as Table. 3 and 5 in the main text.

S1.2. Estimation of $p_{out} = p^2$

To estimate the approximated value of $p_{out} = p^2$, the pressure contour obtained from the 3D simulation is studied. As shown in Fig. S3a-c, the simulated pressure distribution curve along the x direction in the outlet channel can be well approximated by a half parabola that has axis of symmetry at $x = L$ and vertex at $p = p^2$, and passes through the origin, with mathematical function as:

$$p(x) = \frac{p^2}{L^2} (x - L)^2 + p^2 \quad (0 \leq x \leq L) : \quad (S3)$$

Further investigation demonstrated that this approximation agrees with the 3D simulations across permeability ranging from $1 \cdot 10^{-12} \text{ m}^2$ to $1 \cdot 10^{-9} \text{ m}^2$, as shown in Fig. S4. Assuming Eq. (S3) holds regardless of working condition or cell configuration, it is easy to find the value of $p_{out} = p^2$ as follows:

$$\frac{p_{out}}{p^2} = \frac{\int_0^L p(x) dx}{p^2} = \frac{2}{3} : \quad (S4)$$

Combining Eq. (S4) and Eq. (S1), we obtain an approximated analytical equation for \bar{p}_{out}/p_{in} , as stated in Eq. (63) in main text.

Figure S3: (a) Pressure contour of the entire IDFF negative half-cell, obtained from the 3D simulation at 10 mL min^{-1} , (b) emphasized top view of (a) for an arbitrary outlet channel, (c) pressure distribution along x direction in the outlet channel depicted in (b) as well as the fitted parabola.

Figure S4: Pressure distribution along x direction in the outlet channel depicted in Fig. S3b at different permeabilities: (a) $\mu = 1 \cdot 10^{-12} \text{ m}^2$, (b) $\mu = 1 \cdot 10^{-10} \text{ m}^2$, and (c) $\mu = 1 \cdot 10^{-9} \text{ m}^2$. $p^?$ refers to pressure at the entrance of a outlet channel. All the data are obtained from 3D simulations at 10 mL min^{-1} .

S2. Geometric Discretization of the Models

S2.1. Mesh Details

The unstructured meshes used to discretize the 3D and the 2D models are given in detail as Figs. S5–S7. Finer elements are prescribed in the sharp corners, boundaries, etc. to capture the possible steep variations. As shown in Fig. S6b, for the local mesh refinement, the membrane is not discretized as it does not participate the fluid dynamic process.

Figure S5: Meshing of the 3D model with global mesh refinement: (a) the 3D view; (b) a local enlarged view.

Figure S6: Meshing of the 3D model with local mesh refinement for the fluid dynamic responses: (a) the 3D view; (b) a local enlarged view.

S2.2. Mesh Refinement Study

The mesh refinement study is performed by comparing the result of the current density and the pressure drop responses with different meshes, which are characterized by their number of elements.

Figure S7: Meshing of the 2D model: (a) the overall domain; (b) a local enlarged view.

The results are shown as Figs. S8–S10. All the data are obtained at 10 mL min^{-1} and 0.1 V and the presented finest mesh with the largest number of elements is set to the reference mesh for each case. Furthermore, due to symmetry, for the fluid dynamic responses, only the negative half-cell part are presented. As shown in Figs. S8–S10, it can be seen that the mesh used in the model is sufficiently fine with negligible discretization errors ($< 0.1\%$ with respect to the corresponding reference mesh).

Figure S8: Comparison of the resultant current densities at 10 mL min^{-1} and 0.1 V obtained from 3D simulations with different mesh sizes, which are characterized by the number of elements. These meshes correspond to the global mesh refinement in main text.

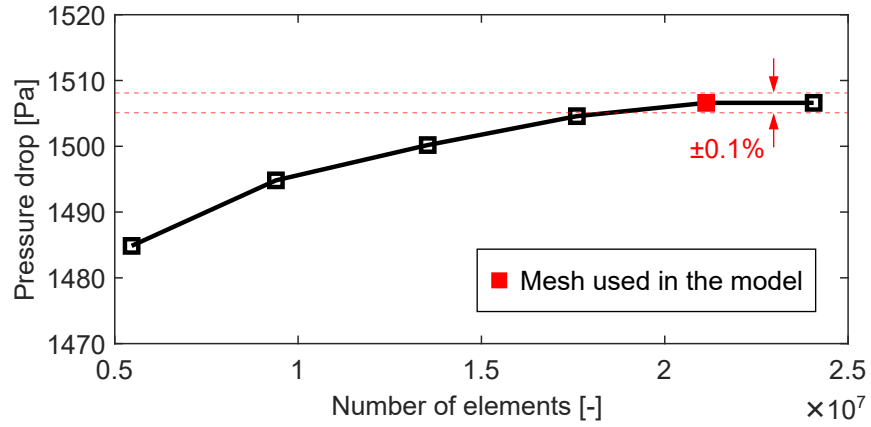


Figure S9: Comparison of the resultant negative half-cell pressure drop at 10 mL min^{-1} obtained from 3D simulations with different mesh sizes, which are characterized by the number of elements. These meshes correspond to the local mesh refinement, which is used to increase the accuracy of the fluid dynamic responses, in main text.

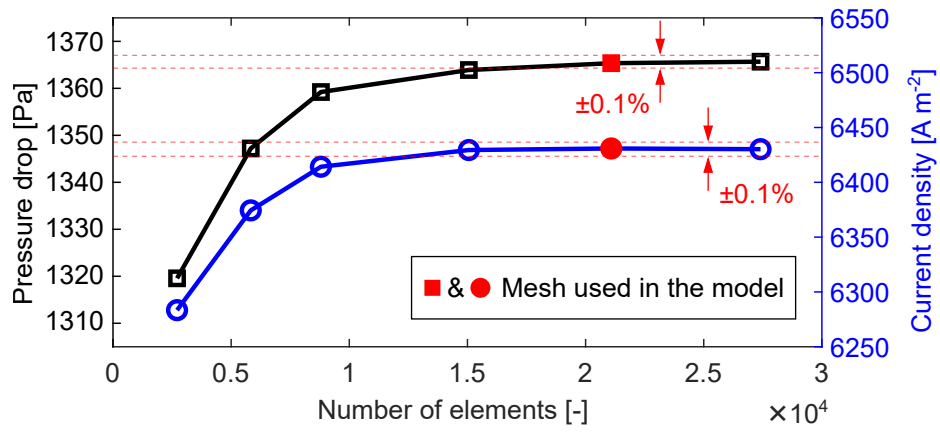


Figure S10: Comparison of the resultant current density and negative half-cell pressure drop at 10 mL min^{-1} and 0.1 V obtained from 2D simulations with different mesh sizes, which are characterized by the number of elements.

S3. Fitting Results

The 3D model was fit to the experimental data by adjusting the negative standard rate constant (i.e., k^-), the ionic conductivity of the membrane (i.e., $\sigma_{l,mem}$), and the pre-factor parameter for mass transfer coefficient (i.e., b) to minimize the discrepancy in current density for fixed cell voltages. The frequency of the residuals from the fit are shown in Fig. S11. It can be observed that the fit exhibit a Gaussian-like distribution around a zero residual. This is indicative of a good fit; however, there are still outliers for the fit. These can be attributed to the discrepancy of the open-circuit voltage (OCV) prediction, as stated in the main text.

Figure S11: The residuals of the curve fitting between the 3D model with the experimental data.

S4. Comparisons of 2D and 3D Simulations

Apart from Fig. 7 in the main text, where the comparison of the fluid dynamic responses and electrochemical responses at 0:1 V is presented, further comparisons of the electrochemical responses at 0:5 V, 0:9 V, and 1:3 V are shown in Figs. S12–S14, respectively. Furthermore, the comparisons of fluid dynamic responses as well as pressure drop prediction for different flow rates ($1\text{--}15\text{ mL min}^{-1}$) between the 2D and 3D models are shown in Figs. S15–S17.

Figure S12: Comparison of the electrochemical responses between the 2D and 3D simulations at 10 mL min^{-1} and 0:5 V: (a) concentration of V^{2+} , (b) liquid-phase electric potential, (c) solid-phase electric potential, and (d) overpotential. Only the negative half cell is shown.

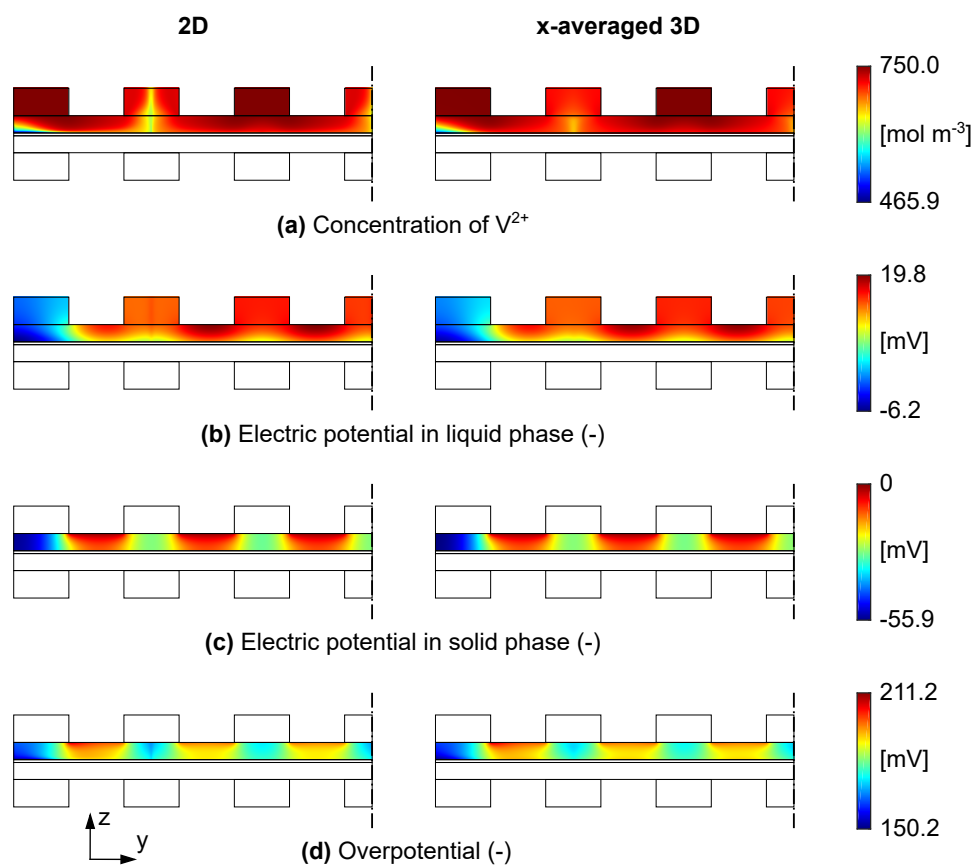


Figure S13: Comparison of the electrochemical responses between the 2D and 3D simulations at 10 mL min^{-1} and 0.9 V : (a) concentration of V^{2+} , (b) liquid-phase electric potential, (c) solid-phase electric potential, and (d) overpotential. Only the negative half cell is shown.

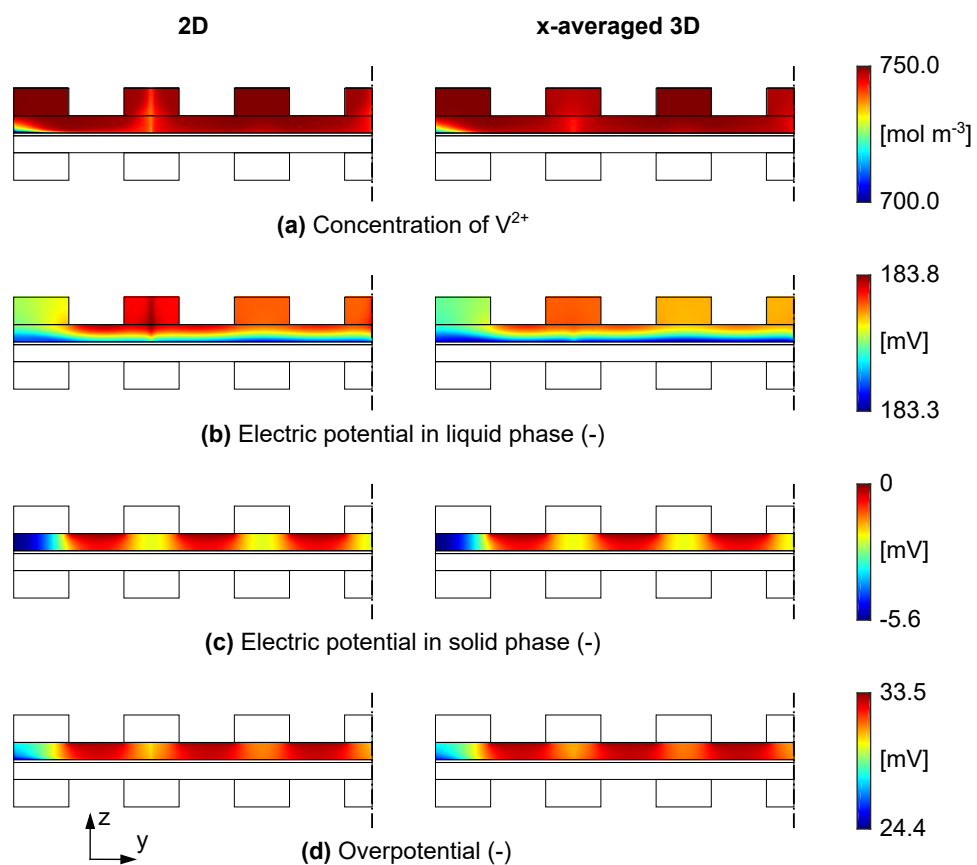


Figure S14: Comparison of the electrochemical responses between the 2D and 3D simulations at 10 mL min^{-1} and 1.3 V : (a) concentration of V^{2+} , (b) liquid-phase electric potential, (c) solid-phase electric potential, and (d) overpotential. Only the negative half cell is shown.

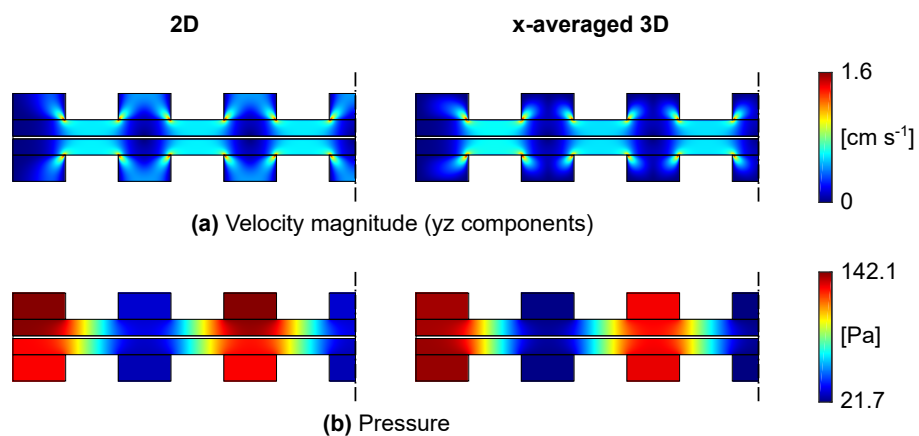


Figure S15: Comparison of the fluid dynamic responses between the 2D and 3D simulations at 1 mL min^{-1} : (a) velocity magnitude (yz components), (b) pressure.

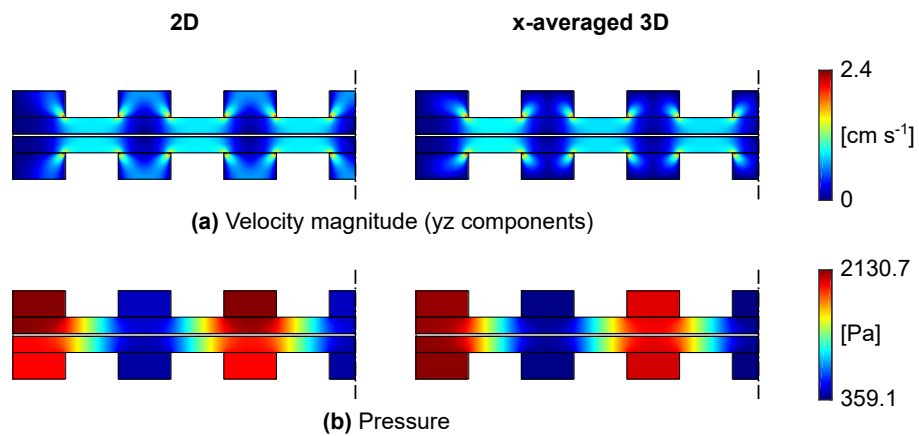


Figure S16: Comparison of the fluid dynamic responses between the 2D and 3D simulations at 15 mL min^{-1} : (a) velocity magnitude (yz components), (b) pressure.

Figure S17: Comparison of the pressure drop between the 2D and 3D simulations at different flow rates. Q_{ref} refers to the reference flow rate which is set to 10 mL min^{-1} . “3D (x -avg.)” means that the 3D pressure drop presented here is the x -averaged value, as shown in Figs. S15 and S16.

S5. Scale-up Study on the \bar{p}_{out} Estimation

The result of the scale-up work on the \bar{p}_{out} estimation (i.e., Eq. (62) in main text) is shown as Fig. S18. It can be seen that even though Eq. (62) only works well for a limited L range (i.e., approximately 0–2 cm), better performance across the entire range can be achieved by increasing the value of θ , for example, the estimation with $\theta = 6$ gives an acceptable \bar{p}_{out}/p_{in} prediction with relative error lower than 5% at $L = 5$ cm. It suggests the ability of our \bar{p}_{out} estimation method to be used for larger cells.

Figure S18: Comparison of $\bar{p}_{out} = p_{in}$ between the 3D simulations and the estimation with different θ for different channel length. Est. indicates the estimation.

S6. Velocity Distributions in Electrode

The variation of the average superficial intraelectrode velocity (yz components) with respect to electrode thickness ($H_{e,-}$), porosity (ε_-), and fiber diameter ($d_{f,-}$), is shown in Fig. S19. The average superficial intraelectrode velocity (yz components) is nondimensionalized by the Reynolds number (Re) as follows [3]:

$$Re = \frac{\rho_- \overline{|\mathbf{u}_{e,2D}|} L}{\mu_-}, \quad (\text{S5})$$

where $\overline{|\mathbf{j}_{\mathbf{u}_{\mathbf{e};2\text{D}}|}}$ refers to the average magnitude of the superficial intraelectrode velocity obtained from the 2D simulations (yz components). It can be seen from Fig. S19 that the intraelectrode velocity does not appreciably change with the porosity or fiber diameter. This qualitatively agrees with estimation reported in Ref. [4], where the average superficial intraelectrode velocity in all three dimensions is estimated as:

$$\overline{|\mathbf{j}_{\mathbf{u}_{\mathbf{e}}|}} = \frac{Q}{NH_{\mathbf{e};-}L}, \quad (\text{S6})$$

with N , $H_{\mathbf{e};-}$, and L being geometrical parameters. We further compared our simulation results with their estimation (i.e., Eq. (S6)), as depicted in Fig. S20, showing good match both qualitatively and quantitatively. The significant difference located in the low $H_{\mathbf{e};-}W_-^{-1}$ region might be attributed to the contribution in x direction, which cannot be covered in this work. To remove the slight influence from ε_- and $d_{\text{f};-}$, the obtained data for $\overline{|\mathbf{j}_{\mathbf{u}_{\mathbf{e};2\text{D}}|}}$ from the simulations has been averaged against ε_- and $d_{\text{f};-}$.

Figure S19: The average superficial intraelectrode velocity magnitude (normalized as Reynolds number Re) as function of the $d_{\text{f};-}$ and the ε_- for respective $H_{\mathbf{e};-}$ values of (a) $1 \cdot 10^{-4}$, (b) $7 \cdot 10^{-4}$, and (c) $20 \cdot 10^{-4}$ m. Additionally, the Re as function of the $d_{\text{f};-}$ and the $H_{\mathbf{e};-}$ for respective ε_- values of (d) 0.60, (e) 0.75, and (f) 0.90. The subscript “ $-$ ” referring to negative electrode is neglected in the figure.

Figure S20: Comparison of the average inraelectrode velocity magnitude (normalized as Reynolds number) obtained from simulations in this work and estimations from a previously reported study in Ref. [4] with respect to different electrode thicknesses (normalized as $H_{e,-} W^{-1}$). The subscript “ $-$ ” referring to negative electrode is neglected in the figure.

S7. Kendall Rank Correlation Coefficient

The numerical values used in generation of Fig. 10 are shown in Tables S1–S4. These values were obtained using the `corr` function in MATLAB, while employing the “Kendall” calculation. All values are rounded to two values after the decimal point.

Table S1: The Kendall rank correlation coefficients for the current density for different cell voltages. These correspond to Fig. 10a in the main text.

U_{cell} [V]	$H_{e,-}$	"	$A_{V,-}$	k
0:30	0:33	0:12	0:54	0:07
0:50	0:26	0:17	0:58	0:13
0:70	0:25	0:18	0:57	0:16
0:90	0:25	0:18	0:55	0:21
1:10	0:26	0:16	0:53	0:27
1:30	0:28	0:15	0:49	0:31

Table S2: The Kendall rank correlation coefficients for η for different cell voltages. These correspond to Fig. 10b in the main text.

U_{cell} [V]	H_{e_i}	"	A_{V_i}	k
0:30	0:26	0:16	0:58	0:12
0:50	0:26	0:17	0:58	0:13
0:70	0:25	0:18	0:57	0:16
0:90	0:25	0:18	0:55	0:21
1:10	0:26	0:16	0:52	0:27
1:30	0:28	0:15	0:49	0:31

Table S3: The Kendall rank correlation coefficients for η for different cell voltages. These correspond to Fig. 10c in the main text.

U_{cell} [V]	H_{e_i}	"	A_{V_i}	k
0:30	0:43	0:03	0:57	0:14
0:50	0:43	0:04	0:56	0:15
0:70	0:44	0:05	0:54	0:16
0:90	0:44	0:05	0:52	0:20
1:10	0:43	0:05	0:50	0:25
1:30	0:43	0:05	0:48	0:29

Table S4: The Kendall rank correlation coefficients for the fluid dynamic outputs. These correspond to Fig. 10d (ρ) and e (k_{m_i}) in the main text.

	H_{e_i}	"	d_f
Pressure drop, ρ	0:59	0:03	0:48
Mass transfer coefficient, k_{m_i}	0:97	0:01	0:07

References

- [1] C. K. Alexander, M. N. O. Sadiku, Fundamentals of Electric Circuits, 5th Edition, McGraw-Hill, New York, NY, 2013.
- [2] E. Cheever, SCAM- A tool for symbolically solving circuit equations, <https://www.mathworks.com/matlabcentral/fileexchange/3443-scaml-a-tool-for-symbolically-solving-circuit-equations> (2020).
- [3] H. K. Versteeg, W. Malalasekera, An Introduction to Computational Fluid Dynamics: The Finite Volume Method, 2nd Edition, Pearson Education Ltd, Harlow, England ; New York, 2007.
- [4] R. M. Darling, M. L. Perry, The Influence of Electrode and Channel Configurations on Flow Battery Performance, Journal of The Electrochemical Society 161 (9) (2014) A1381–A1387. doi:10.1149/2.0941409jes .